A parametric life-cycle model for assessing environmental impacts of 4G and 5G cellular base stations: Online Resource 1

Louis Golard*, louis.golard@uclouvain.be
Robin Dethienne*, robin.dethienne@uclouvain.be
Jérôme Louveaux*, jerome.louveaux@uclouvain.be
David Bol*, david.bol@uclouvain.be

*ICTEAM – UCLouvain, Louvain-la-Neuve, Belgium

This document contains supplementary information to the paper published in *The International Journal of Life Cycle Assessment*. After presenting an overview of cellular base stations (BSs) in Section 1, Section 2 provides detailed pictures of our own teardowns and links to external teardowns. In Section 3, we explain how regression analyses are performed based on the specific data sources for modeling the foreground process inventory (FPI) and we provide equations of all parametric functions of the FPI with the associated estimates of numerical parameters. In Section 4, we detail how we build background processes to calculate impact assessment factors (IAFs), in some cases based on custom unit processes. Then, Section 5 provides details on how the uncertainty factors are calculated, and Section 6 explains the calculations of data throughput capacity and coverage of typical BS configurations. Finally, additional results of the LCA study are presented in Section 7.

Table of Contents

1 Overview of cellular base stations 2
2 Teardowns of base station components 3
2.1 Own teardowns 3
2.2 External teardowns 6
2.3 Additional information 7
3 FPI: regression analyses 10
3.1 Production stage modules 10
3.2 Distribution stage module 19
3.3 Use stage module 20
3.4 End-of-life stage module 21
4 IAF calculations 22
4.1 Custom unit processes for electronic sub-components 22
4.2 Modeling assumptions for metal and polymer processing 26
4.3 Composition of electronic sub-components 27
4.4 Composition of mechanical sub-components 29
5 Uncertainty quantification 31
5.1 Uncertainty factors for the FPI 31
5.2 Uncertainty factors for IAFs 34
6 Base station capacity and coverage 35
6.1 Capacity computation 35
6.2 Coverage computation 35
7 Additional results 37
7.1 IAF results 37
7.2 Assessment of all life-cycle stages 38

1 Overview of cellular base stations

This LCA study builds on a simplified and modular representation of BSs. We propose in Figure 1 a simplified overview of a BS as the basic physical node constituting the cellular radio access network. It connects user equipment to the Internet network via the mobile core network, and it is controlled by the control network. The BS comprises communication components handling communication-specific functions and support components handling other non-specific functions. In this study, only the components required to operate the BS are included in the scope, thereby excluding ancillary components and building elements such as the pylon. Then, in Figure 2, we propose a simplified division of a generic BS into active and passive functional blocks that perform the various functions required to provide wireless mobile Internet access as with 4G-LTE and 5G-NR. Please note that, although based on illustrations shown in Figure 1 and Figure 2, our LCA study may differ in the definition of LCA modules, BS components and BS sub-components.

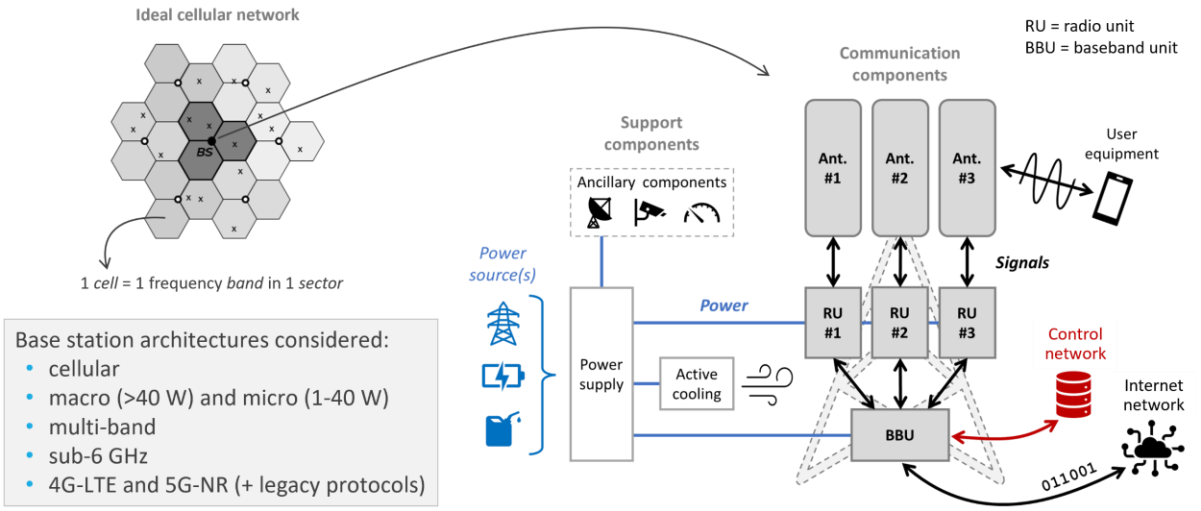

Fig. 1 Simplified overview of a base station (and its main components) as the basic physical node constituting the cellular radio access network and connecting user equipment to the Internet network

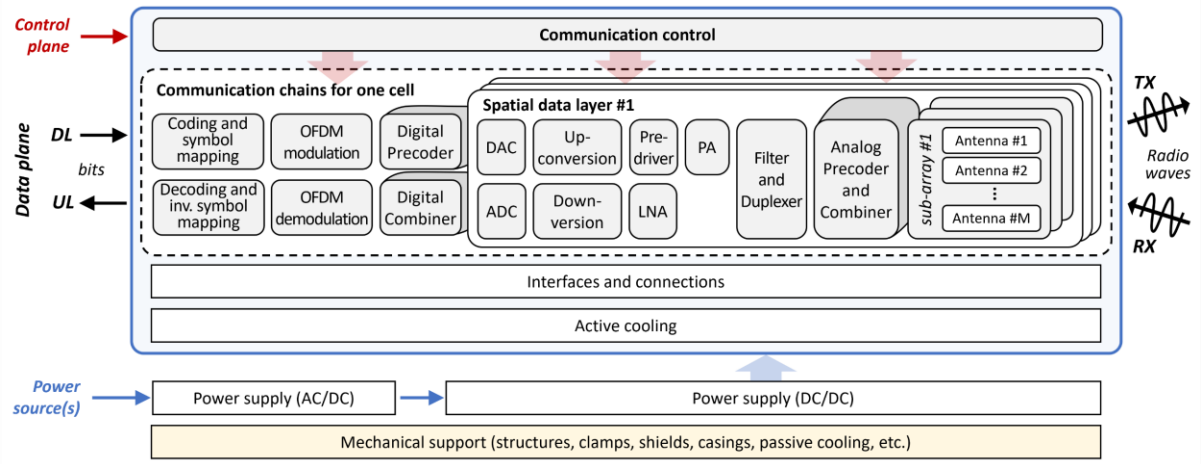

Fig. 2 Simplified division of a base station into active and passive functional blocks performing the various functions required to provide wireless mobile Internet access

2 Teardowns of base station components

This LCA study relies on three types of specific data sources: (i) teardowns of BS components, (ii) technical documentation from BS manufacturers, and (iii) data and information from network operators. This section first details our own teardowns of BS components and then lists the additional sources that provide external teardowns for various other BS configurations. Full technical documentation from BS manufacturers and information from network operators cannot be published for confidentiality reasons. Yet, we disclose some elements of these sources if they are helpful. In that case, manufacturers and vendors are deliberately anonymized.

2.1 Own teardowns

We have performed our own teardowns of a BBU, a RRU, and a traditional passive AU. These BS components were installed on a cellular macro-BS deployed in an urban area of a Belgian city. In 2022, this BS supported three sectors and four frequency bands (i.e., 12 cells), all implementing 2T2R FDD protocols:

- 2G-GSM at 0.9 GHz with 10 MHz of bandwidth.
- 3G-UMTS at 2.1 GHz with 15 MHz of bandwidth.
- 4G-LTE at 0.8 GHz with 10 MHz of bandwidth.
- 4G-LTE at 1.8 GHz with 20 MHz of bandwidth.

This BS featured multiple radio access technology (multi-RAT) allowing cells initially configured for 3G-UMTS and 4G-LTE to support both protocols. The components of this BS were produced and installed in the 2010s.

We were able to get and tear down these components because the network operator de-installed them in 2022 in order to upgrade the BS with new and up-to-date components while deploying 5G-NR. The operator then gave us these old components, which had reached their end-of-life. By tearing down these components, we were able to get any kind of details we need for the LCA study. In the following, we describe all these BS components.

2.1.1 Baseband unit

The BBU under study consists of a modular sub-rack that can house different types of boards in several slots, as shown in Figure 3(a) and Figure 3(b). The BBU processes baseband signals of the BS and comprises the following subsystems: baseband subsystem, power subsystem, transmission subsystem, interconnection subsystem, main control subsystem, monitoring subsystem, and clock subsystem. A backplane connects all these subsystems together. The schematic diagram of the BBU working principle is shown in Figure 3(c). In the case of this specific BS, the BBU comprises 8 boards occupying 9 slots:

- Slots 5, 6 and 7: two boards handling the link-layer operations for all cells of the BS, one specific to 2G-GSM and the other to 3G-UMTS and 4G-LTE. They process BS signaling and manage resources for other BBU boards.
- Slots 0, 2 and 3: three boards handling the physical-layer operations for all cells of the BS, one specific to 4G-LTE and the other two generic for 2G-GSM, 3G-UMTS and 4G-LTE. They process downlink (DL) and uplink (UL) baseband signals and implement multi-RAT.
- Slot 8, 9 and 10: three boards handling miscellaneous functions such as power conversion (from -48 V DC to +12 V DC), power management and heat dissipation through fans.

Figure 4 shows pictures of the complete BBU assembled in the sub-rack, as well as pictures of different boards removed from the sub-rack. The total mass of the complete BBU is 9.7 kg.

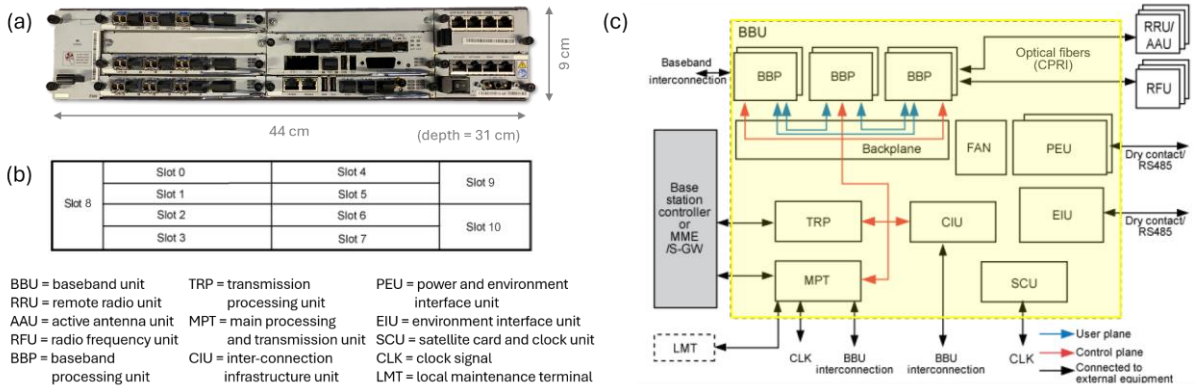

Fig. 3 Overview of the BBU under study: (a) picture of the BBU front panel with 9 slots occupied and others empty, (b) diagram of all available slots, and (c) diagram of the working principle [adapted from BS manufacturers' technical documentation]

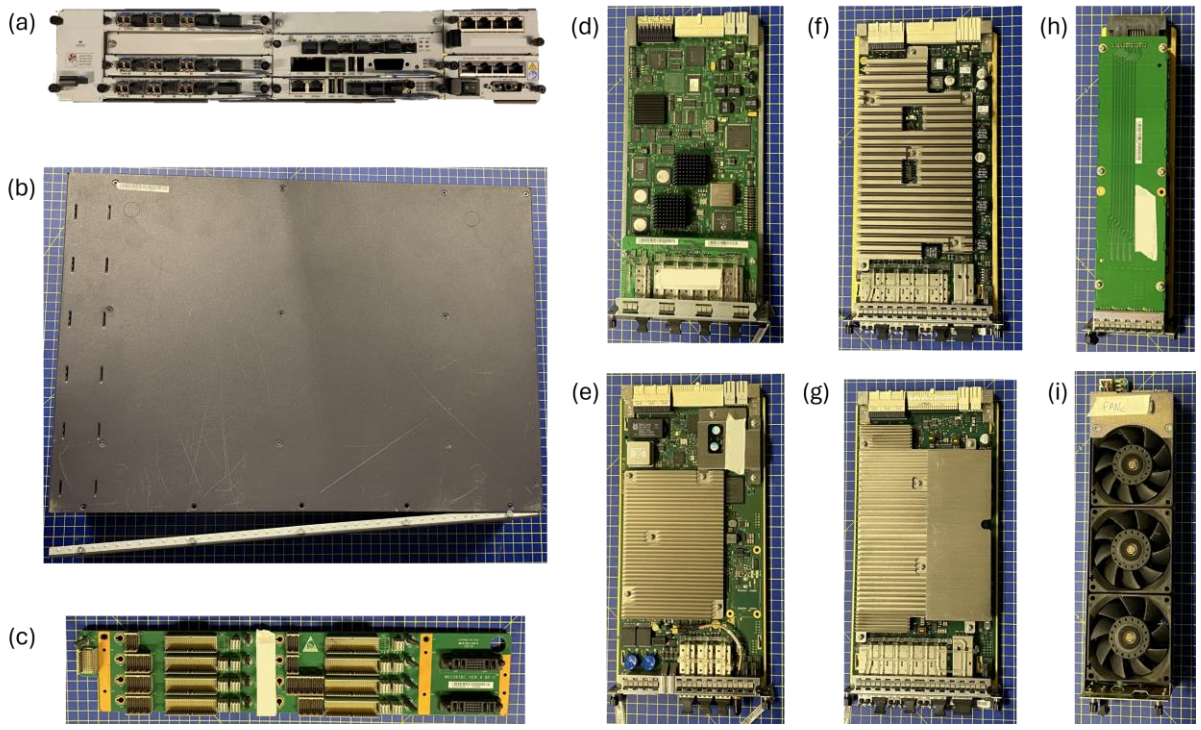

Fig. 4 Pictures of the teardown of the BBU: (a) the front interface of the complete BBU, (b) the sub-rack casing from above, (c) the backplane located at the rear of the sub-rack, (d) the link-layer board specific to 2G-GSM, (e) the other link-layer board, (f) the physical-layer board specific to 4G-LTE, (g) one of the other physical-layer boards, (h) the board handling the power conversion and management, and (i) the board containing the fans

2.1.2 Radio unit

The RU under study is a remote RU (RRU) comprising a high-speed interface unit (i.e., a CPRI connection), a signal processing unit, power amplifiers, a duplexer, and a power module as shown in Figure 5. In the DL communication chain, the RRU receives DL baseband signal from the BBU, performs digital-to-analog conversion, up-converts and amplifies transmit (TX) signals. In the UL chain, the RRU receives radio frequency (RF) signals from the AU, down-converts and amplifies these receive (RX) signals, performs analog-to-digital conversion, and sends UL baseband signal to the BBU. In addition, it filters and multiplexes RX and TX signals on the RF channel, which enables these signals to share the same antenna path.

This RRU supports communication protocols from 2G-GSM to 4G-LTE on the 1.8 GHz frequency band with a bandwidth of up to 20MHz and implements FDD in a 2T2R configuration. Its maximum output power per TX chain is 40 W, enabling a complete configuration of 2×40 W. Figure 6 shows pictures of the complete RRU, as well as pictures of its opening and various internal sub-components. The total mass of the RRU is 15 kg.

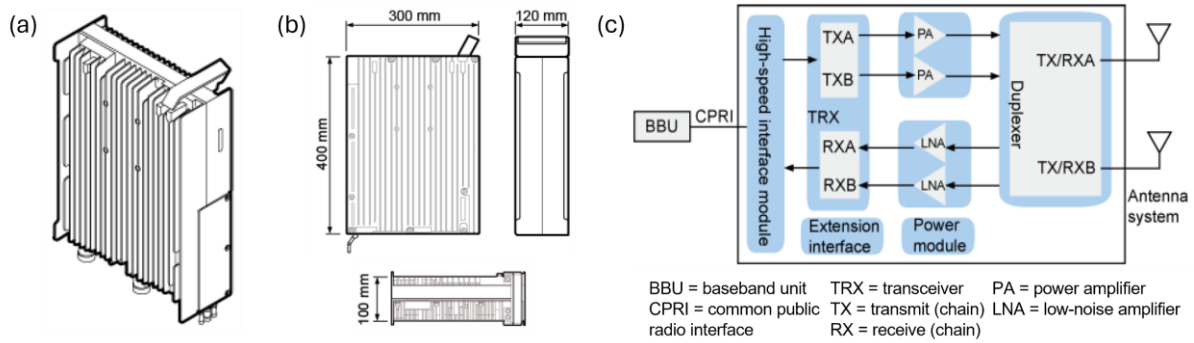

Fig. 5 Overview of the RRU under study: (a) exterior view, (b) outer dimensions, and (c) diagram of the working principle [adapted from BS manufacturers' technical documentation]

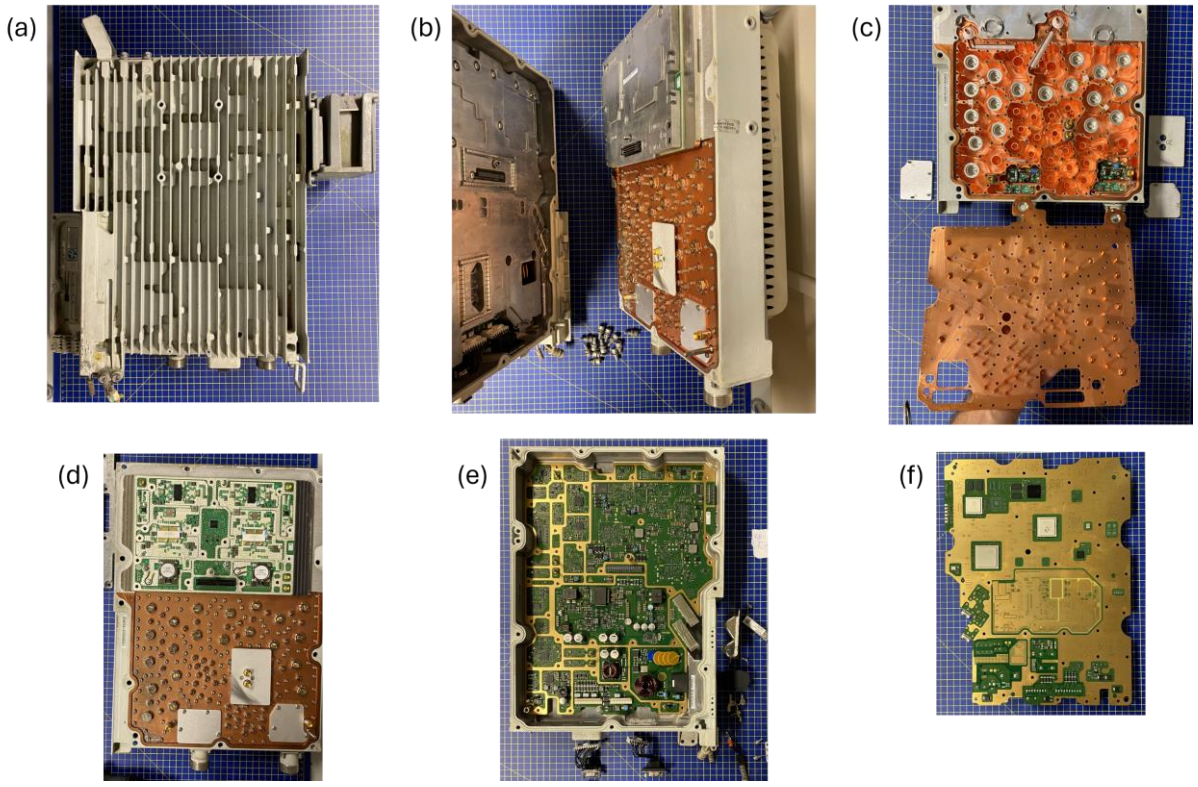

Fig. 6 Picture of the teardown of the RRU: (a) the side view of the complete RRU, (b) its two main parts once opened, (c) the disassembled cavity filters connected to the two external coaxial connectors, (d) the PCBA comprising the two power amplifiers (one per layer and hence per TX channel) above the duplexer and filters, (e) the front of the main PCBA, and (f) the rear of the main PCBA

2.1.3 Antenna unit

The traditional AU under study transmits and receives RF signals as radio waves to and from user equipment (see Figure 7(a)). It superimposes two antenna arrays transmitting in two frequency ranges: 0.7-1.0 GHz and 1.7-2.7 GHz. The low-frequency antenna array is divided into two vertical sub-arrays (in red in Figure 7(b)) made up of eight AEs, each supporting two cross-polarized channels (i.e., 2T2R). The high-frequency antenna array is divided into four vertical sub-arrays (in yellow in Figure 7(b)) made up of seven or eight AEs, each supporting 2T2R cross-polarized channels. This explains the availability of $2 \times 2 = 4$ coaxial connectors for the low-frequency range, plus $4 \times 2 = 8$ coaxial connectors for the high-frequency range (see Figure 7(c)). Note that not all sub-arrays in the same frequency range have to carry the same frequency band (but can do so). This would allow this AU to support, e.g., two 2T2R frequency bands at 0.8 and 0.9 GHz, two 2T2R frequency bands at 1.8 and 2.1 GHz, and a 4T4R frequency band at 2.6 GHz. The total antenna gain of the AU is around 16 dBi, which is explained by the 7 or 8 AEs per sub-array, resulting in an array gain of the sub-arrays of about 9 dB, to which the individual gain of each AE must be added, approximately 7 dBi. The AU does not support ABF since the horizontal spacing between sub-arrays is greater than 0.5, which means that signals from different sub-arrays cannot be combined constructively to form beams with higher gain. Only spatial multiplexing of multiple MIMO layers is therefore possible with this AU. The horizontal half-power beamwidth (HPBW) of the AU is about 60°, and the vertical HPBW is about 10° (see Figure 7(d)).

The AU can be connected to multiple RUs through coaxial cables via the external coaxial connectors. RF signals are handled internally by smaller coaxial cables and RF delay lines. This AU also features a remote electrical tilt (RET) system used to remotely adjust the electrical down-tilt of AU beams. Yet, this feature is not considered in our LCA study, and the RET system is hence excluded from the modeling. Figure 8 shows pictures of different main parts of the AU. The total mass of the AU is 38 kg including the clamps.

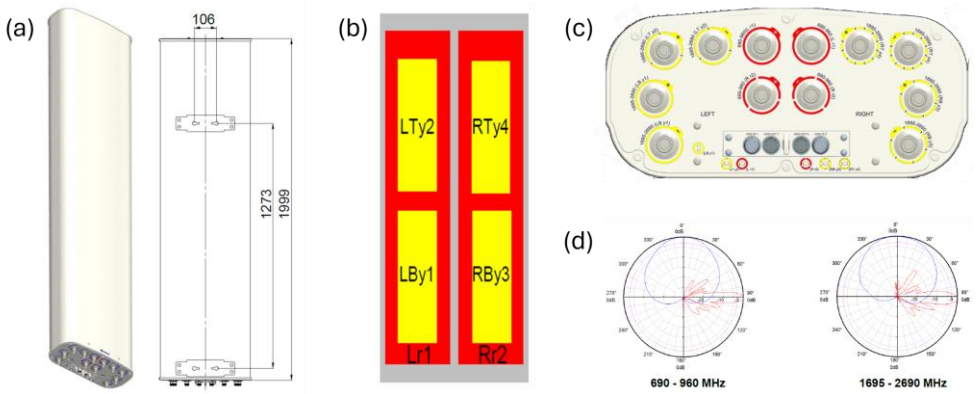

Fig. 7 Overview of the AU under study: (a) exterior view and outer dimensions, (b) diagram of sub-array layout, (c) interface panel with coaxial connectors, and (d) horizontal (in blue) and vertical (in red) radiation patterns for both frequency ranges [adapted from BS manufacturers' technical documentation]

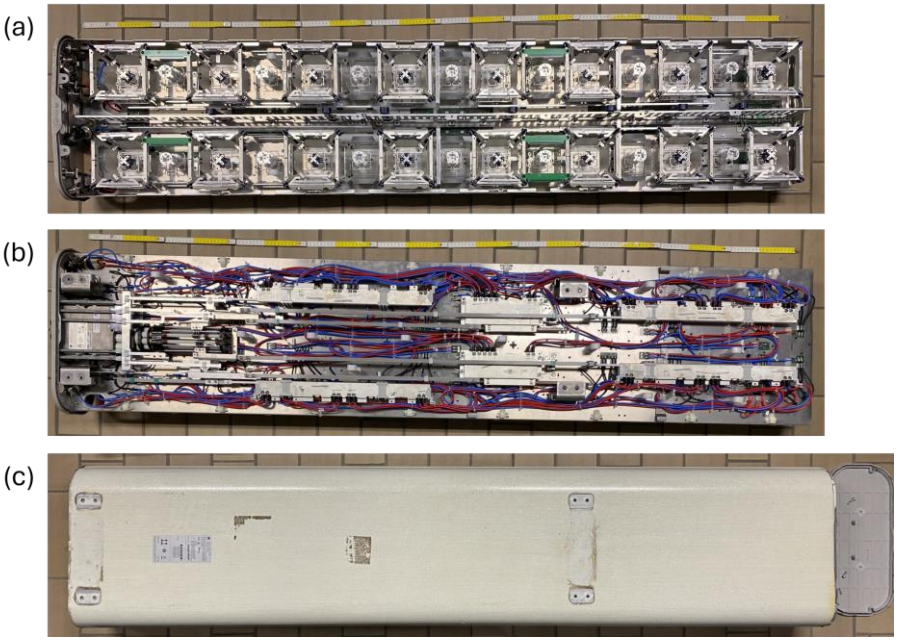

Fig. 8 Picture of the teardown of the traditional AU: (a) the antenna arrays made up of multiple antenna elements, (b) the rear of the AU with the internal coaxial cables, the delay lines and the remote electrical tilt system, and (c) the radome in reinforced polymer

2.2 External teardowns

In addition to our own teardowns, we use external teardowns that are publicly available. These data sources cover several BS components from various manufacturers (Huawei, Nokia, Ericsson, etc.) and provide description and pictures of disassembled BS components.

For RUs, we use following sources (see Table 1):

(1) **FCC Database** (https://fcc.report/FCC-ID/ and https://fccid.io/): All wireless emitting devices sold in the USA require an FCC ID. The FCC Database gathers, among other things, internal pictures of these devices (note that they are not available for all devices).
(2) **Mads Barnkob** (https://kaizerpowerelectronics.dk/teardown/, https://highvoltageforum.net/ and https://www.youtube.com/@KaizerPowerElectronicsDk): Mads Barnkob runs a Youtube channel and a website, and performs experiments with power electronics, inverters and high voltage equipment. In addition, he also teardowns and studies BS components.
(3) **Yole group** (https://www.yolegroup.com/product/report/ericsson-5g-integrated-radio-unit-air6488-chipset/): Yole group provides, among other things, reverse engineering services. Their reports are subject to a fee, but it is possible to access previews of selected sections.

For the power converter of a PSU: http://www.ea1ddo.es/Eltek_FlatPack2/Eltek_FlatPack2.html

Table 1 Sources of external teardowns of RUs with their specifications

Source	Type	Manufacturer	Name	Supported protocols	Frequency band [GHz]	TX/RX config.	TX power per PA [W]
(1)	micro-RRU	ZTE	BS8922S1900	3G	1.9	2T2R	5
(1)	RRU	ZTE	R8862AS600	2G-4G	2.6	2T4R	40
(1)	RRU	Huawei	RRU5303	4G	1.9	2T4R	40
(1)	RRU	Huawei	RRU3953	2G-5G	1.8	2T4R	80
(1)	RRU	Huawei	RRU3971	2G-5G	1.8	4T4R	40
(1)	RRU	Huawei	RRU3232	4G	2.6	4T4R	20
(1)	RRU	Huawei	RRU3279	4G	2.6	8T8R	20
(1)	RRU	Huawei	RRU3278	4G-5G	3.5	8T8R	16
(2)	RRU	Huawei	RRU3928	2G-4G	1.8	2T2R	40
(2)	RRU	Huawei	RRU3908	2G-4G	1.8	2T2R	40
(2)	3-sectors RFU	Nokia	FXEB	2G-3G	1.8	1T2R	90
(2)	3-sectors RFU	Nokia	FXEA	2G-3G	1.8	1T2R	70
(2)	3-sectors RFU	Nokia	Flexi WCDMA	2G-3G	2.1	1T2R	80
(2)	RRU	Ericsson	RRU 11 B4	2G-4G	1.8	2T2R	40
(3)	AAU	Ericsson	AIR6488	4G-5G	3.6	32T32R	6.25

2.3 Additional information

For this LCA study, we were unable to access an AAU to tear it down by ourselves because these components are fairly new on the market and have not yet reached their end-of-life. Similarly, PSUs are mostly reused even when the BS is upgraded, so on average they have a longer lifetime than other components. Therefore, in addition to external teardowns, this section provides some additional information from manufacturers' technical documentation to help better understand the architecture and composition of AAUs, PSUs and packaging.

2.3.1 Active antenna unit

An AAU combines the functions of an RU and an AU. Figure 9 shows two diagrams of AAU working principles which explicitly distinguish the RU part from the AU part. Figure 10 shows an exploded view of one particular AAU, including all the sub-components of a RU and an AU.

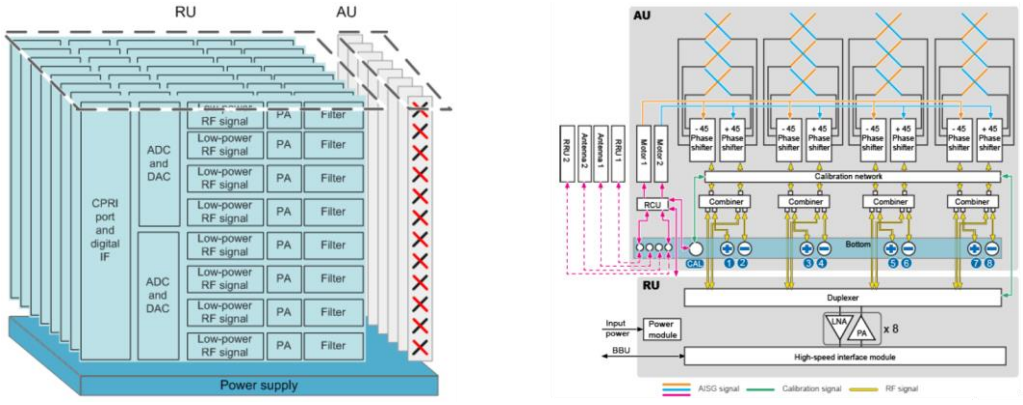

Fig. 9 Examples of two diagrams of AAU working principles distinguishing between the RU and AU parts [adapted from BS manufacturers' technical documentation]

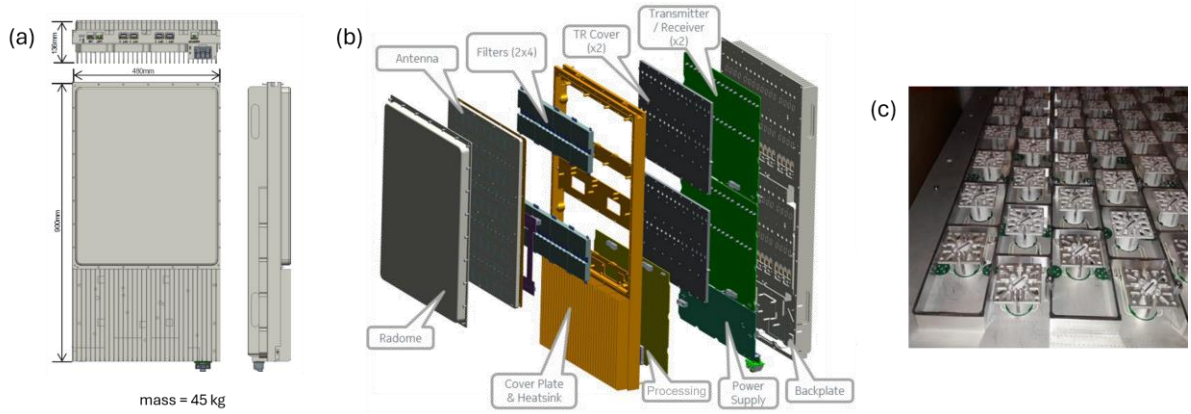

Fig. 10 Overview of one particular AAU: (a) external view and outer dimensions, (b) exploded view of all its sub-components, and (c) picture of its antenna array [adapted from BS manufacturers' technical documentation]

2.3.2 Power supply unit

A PSU for DC power supply of telecom equipment such as a BS is fed from an external AC supply, and consists of multiple rectifiers, a controller and a DC distribution unit. Batteries, fuses and contactors are also part of the system. The controller monitors the whole PSU and serves as the local user interface (see Figure 11). Figure 12 shows pictures of different PSU configurations, either in sub-rack without batteries, or with batteries in a cabinet. Typically, the cabinet can also house the BBU, fans, RFUs, etc.

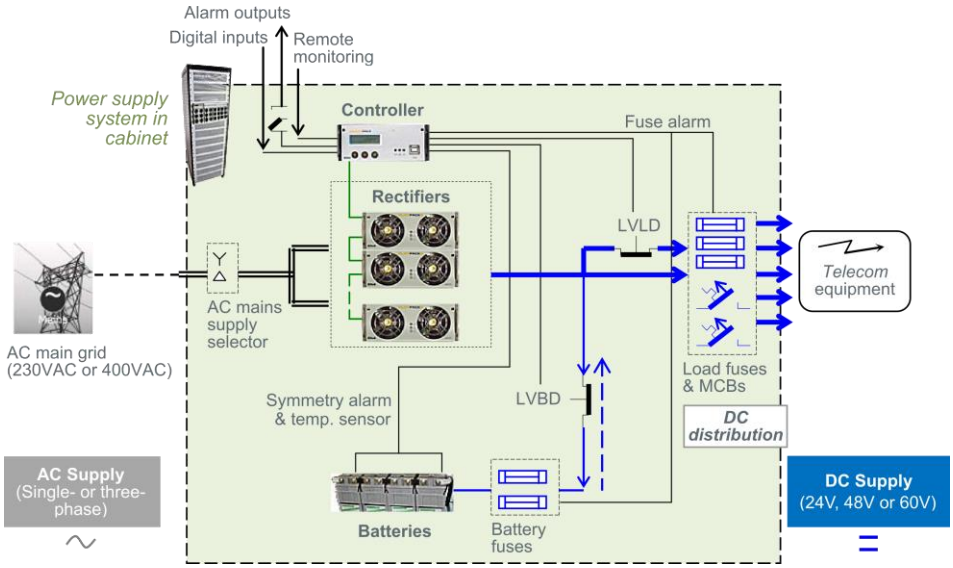

Fig. 11 Working principle of the BS power supply [adapted from BS manufacturers' technical documentation]

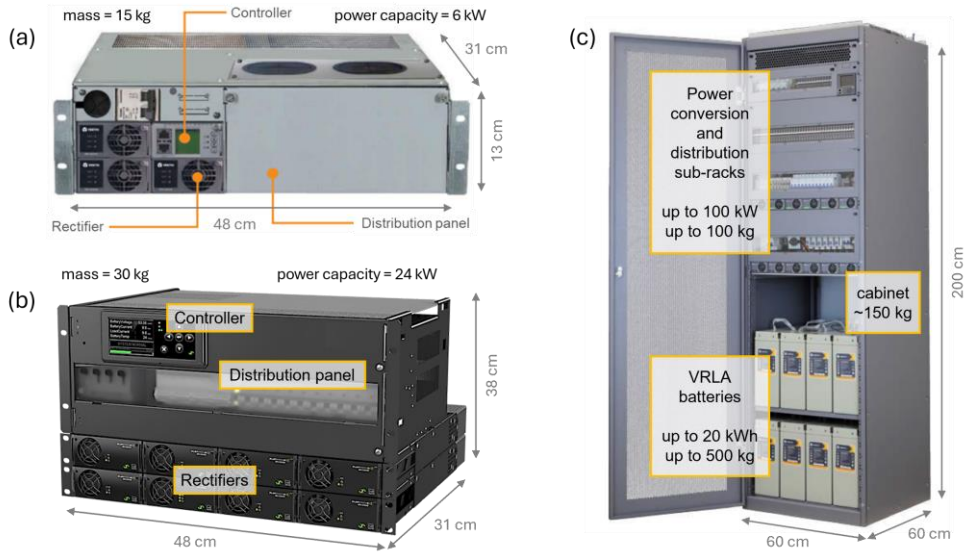

Fig. 12 Overview of different PSU configurations: (a) and (b) pictures of two PSUs in sub-rack, and (c) picture of a PSU with batteries in a cabinet [adapted from BS manufacturers' technical documentation]

2.3.3 Packaging

Typically, BS components are packaged in corrugated cardboard boxes, and plastic bags, protected by laminated paperboard, expanded polystyrene foam and various wooden parts, including pallets (on which one or more components can be placed, depending on their size), as shown in Figure 13.

Fig. 13 Pictures of three BS components in their packaging [adapted from BS manufacturers' technical documentation]

3 FPI: regression analyses

The FPI consists in determining the parametric functions of the foreground process quantities that constitute the vector $Q(x)$ for each module of the life-cycle model. The eight modules of the model represent:

- the production of the BBU,
- the production of the RUs,
- the production of the AUs,
- the production of the PSU,
- the production of the cables,
- the distribution of BS components,
- the use of the BS,
- and the end-of-life of BS components.

In this section, we detail our modeling assumptions and explain how the regression analyses are performed on the basis of the specific data sources. The goodness-of-fit of these regressions is assessed using the root mean square error (RMSE) and the coefficient of determination (R^2).

The figures in this section use different colors to distinguish the type of specific data sources used:

- Red = data from our own teardowns
- Orange = data from external teardowns
- Green = data from equipment documentation
- Blue = data from mobile network operators (MNOs)

Where possible, we also distinguish the variety of vendors using different markers:

- ○ = vendor A (deliberately anonymized)
- □ = vendor B (deliberately anonymized)
- ▽ = all other vendors

3.1 Production stage modules

The foreground processes involved in the production of BS components are grouped into four types:

- the production of electronic sub-components,
- the production of mechanical sub-components,
- the upstream transport of these sub-components from their respective manufacturing factories to the final assembly factory,
- and the final assembly of the component.

Denoting $E(x)$, $M(x)$, $T(x)$ and $A(x)$ the row vectors of process quantities for each of these four process types, the vector $Q(x)$ becomes their horizontal concatenation as

$$Q(x) = [E(x) \quad M(x) \quad T(x) \quad A(x)]\,.$$

This vector applies either to the entire BS or to an individual cell. The following sub-sections detail the parametric functions of these four types of process, as well as numerical estimates of model parameters computed over the validity domain of the model.

In general, we model the production of a sub-component by scaling its quantity as a function of scaling variables relative to a reference situation. Table 2 provides the reference values of scaling variables in the reference situation.

Table 2 Reference situation for sub-component quantity scaling

Scaling variable	Frequency	Bandwidth	Power	Duration	Mass	Surface area
Reference situation	$f^\star = 1$ GHz	$B^\star = 1$ MHz	$P^\star = 1$ W	$\tau^\star = 1$ hour	$\mathcal{M}^\star = 1$ kg	$\mathcal{A}^\star = 1$ cm²

3.1.1 Upstream transport (for all production stage modules)

Due to a lack of primary data, we assume an upstream transport distance $d_{up} = 1000$ km for all sub-components like the standard transport distance of electronic modules in Hischier et al. (2007), with a wide range of uncertainty. Packaging is not modeled as we consider its impacts to be negligible. For a given production stage module, the total freight quantity is the sum of freight for its $\widetilde{K}_i$ electronic plus mechanical sub-components as

$$t_i(x) = d_{up} \sum_{k=1}^{\widetilde{K}_i} q_{k,i}(x)\rho_k \quad [\text{kg} \cdot \text{km}]\,,$$

where $q_{k,i}(x)$ is the quantity of sub-component k in production stage module i, and ρ_k is its mass density of sub-component k if its quantity is not expressed in kg. For instance, we estimate that the mass density of all PCBAs is $\rho_{PCBA} = 0.001$ kg/cm² (see Figure 14).

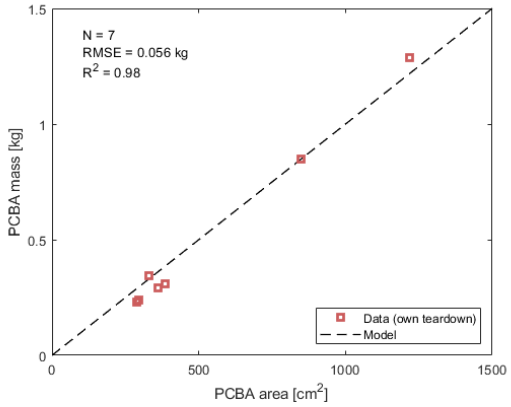

Fig. 14 Mass of different PCBAs in various BS components vs. their areas

3.1.2 Component assembly (for all production stage modules)

The final assembly of BS components is modeled by a given electricity consumption. Again, due to a lack of primary data, we assume the same electricity consumption $a_{elec} = 1000$ Wh for the assembly of any BS component, in the same order of magnitude as Hischier et al. (2007) for the assembly of similar electronic devices, with a wide range of uncertainty.

3.1.3 Baseband unit production

The total number of BBU boards for the entire BS is the sum of the number of link-layer and physical-layer boards. Quantities of both types of board are modeled by e_{link} and e_{phy}, the surface areas of their PCBAs. Based on information from MNOs, we estimate the total PCBA surface area of BBU boards for a large number of BS configurations, knowing their respective number of boards and knowing that the PCBA area is around 650 cm² per board, based on the technical documentation. Table 3 provides the parametric model of BBU production and Figure 15 shows related regression analysis.

The total PCBA area of link-layer boards in the entire BS scales with the square root of the total number of cells N_C (see Figure 15(a)), and we allocate to each cell an equal fraction of these boards by dividing their total area by N_C. The PCBA area of physical-layer boards for one cell scales with the cell capacity (see Figure 15(b)), which depends on B and N_L. An additional parameter, denoted by n_{BBP}, models the number of baseband processing units required for duplexing the downlink (DL) and uplink (UL). The latter varies with the duplex scheme because DL and UL operate simultaneously in frequency division duplex (FDD), but sequentially in time division duplex (TDD). This suggests that a single processing unit could potentially support both the DL and UL in TDD, while two separate units are needed in FDD. We model n_{BBP} by defining τ_{DL} and τ_{UL} as the DL and UL time ratios such that $\tau_{DL} = 1$ in FDD and $\tau_{DL} + \tau_{UL} = 1$ in TDD. Then, we define a degree of differentiation between DL and UL processing units δ_{BBP}, such that $0 \leq \delta_{BBP} \leq 1$. In our model, we assume the median value of $\delta_{BBP} = 0.5$. Although in practice the number of BBU boards must be an integer, which explains the stairs observed in Figure 15(a) and Figure 15(b), the parametric model allows e_{link} and e_{phy} to be any surface area.

An additional area of PCBA e_{misc} is considered for miscellaneous functions such as power management, fan cooling, etc., which is proportional to the sum of e_{link} and e_{phy} (see Figure 15(c)). The total area of BBU PCBAs for the cell is denoted e_{BBU}. The mass m_{BBU} of mechanical parts of BBU boards plus the sub-rack that holds them together scales linearly with e_{BBU} (see Figure 15(d)).

Table 3 Parametric model of BBU production

Foreground process type	Parametric functions of foreground process quantities	Numerical estimates of model parameters
Electronic sub-components	$E_{BBU} = [e_{link} \quad e_{phy} \quad e_{misc}]$ $n_{BBP} = (\tau_{DL}+\tau_{UL}) + (2-\tau_{DL}-\tau_{UL}) \cdot \delta_{BBP}$ $e_{link} = \frac{1}{N_C} e_{link}^{ref} \cdot (N_C)^{\alpha_{link}}$ $e_{phy} = N_L n_{BBP} e_{phy}^{ref} \cdot \left(\frac{B}{B^*}\right)^{\alpha_{phy}}$ $e_{misc} = (e_{link} + e_{phy}) \cdot \delta_{misc}$ $e_{BBU} = e_{link} + e_{phy} + e_{misc}$	$\tau_{DL} = 1$ (FDD) | 0.75 (TDD) $\tau_{UL} = 1$ (FDD) | 0.25 (TDD) $\delta_{BBP} = 0.5$ $e_{link}^{ref} = 320$ cm² $e_{phy}^{ref} = 4$ cm² $\alpha_{link} = 0.5$ $\alpha_{phy} = 0.5$ $\delta_{misc} = 0.15$
Mechanical sub-components	$M_{BBU} = [m_{BBU}]$ $m_{BBU} = m_{BBU}^{ref} \cdot \left(\frac{e_{BBU}}{\mathcal{A}^*}\right)^{\alpha_{BBU}}$	$m_{BBU}^{ref} = 0.003$ kg $\alpha_{BBU} = 1$
Upstream transport	$T_{BBU} = [t_{BBU}]$ $t_{BBU} = d_{up} \cdot (e_{BBU}\rho_{PCBA} + m_{BBU})$	$d_{up} = 1000$ km $\rho_{PCBA} = 0.001$ kg/cm²
Component assembly	$A_{BBU} = [a_{BBU}]$ $a_{BBU} = a_{elec}$	$a_{elec} = 1000$ Wh

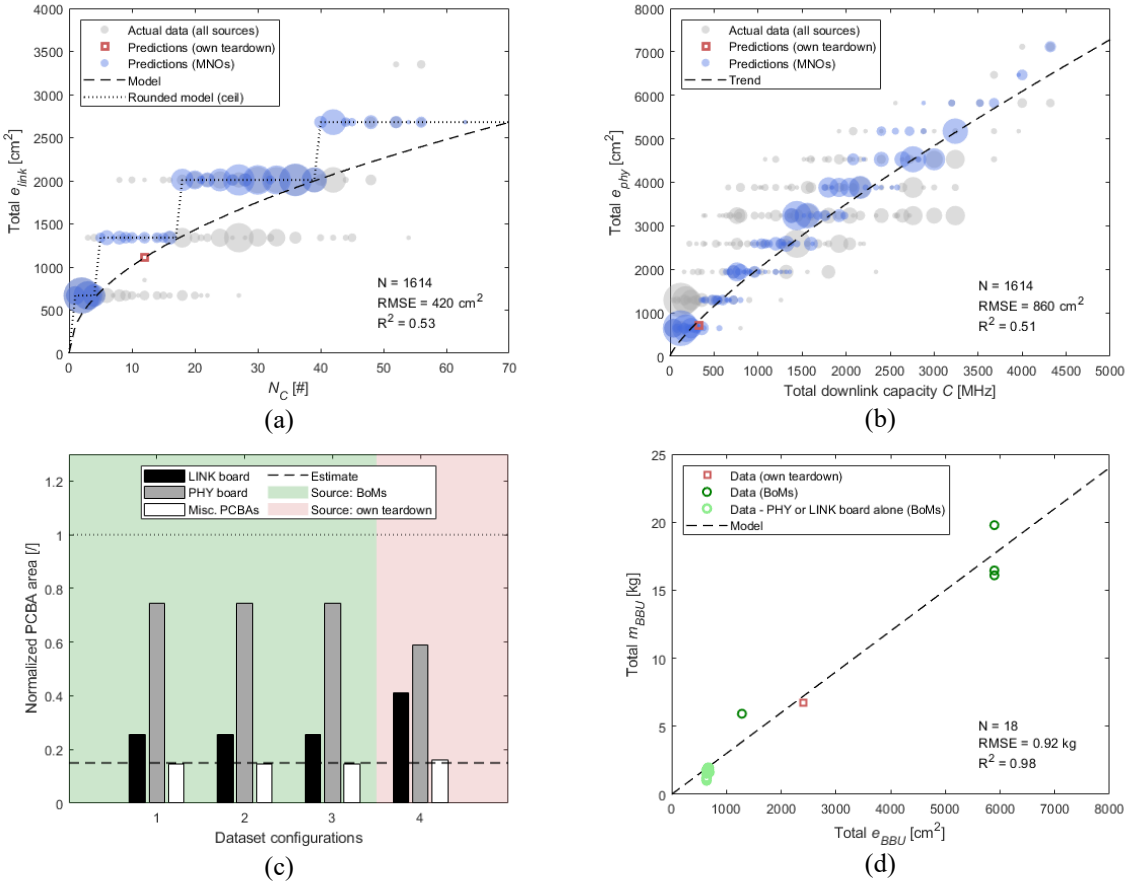

Fig. 15 Regression analysis for the BBU production model: actual and predicted total PCBA area (in the complete BBU for the entire BS) of (a) link-layer boards vs. the total number of cells, and (b) physical-layer boards vs. the total downlink capacity, (c) normalized PCBA area per type of board in different BBU configurations, and (d) total mass of mechanical structure vs. the total PCBA area in the BBU for the entire BS

3.1.4 Radio unit production

The AFE and PA functions are performed by electronic sub-components which we distinguish into four parts: the power supply, the processing units, the transceivers (TRXs) and the amplifiers, whose quantities are modeled by their PCBA areas, respectively e_{sup}, e_{proc}, e_{TRX} and e_{PA}. To model these surfaces, we primarily use the number of TX and RX chains, i.e., N_{TX} and N_{RX}, that are usually the same for a given cell. In that case, they are both equal to N_{TRX}, the number of transceivers (TRXs), such that $N_{TRX} = N_{TX} = N_{RX}$. Otherwise, N_{TRX} is the maximum value between N_{TX} and N_{RX}, such as $N_{TRX} = \max(N_{TX}, N_{RX})$. Furthermore, N_{TRX} must be greater than or equal to N_L in order to spatially separate the data layers. When $N_{TRX} > N_L$, it means that several chains carry the same data layer to implement adaptive beamforming (ABF) as, e.g., in AAUs.

Technical documentation from manufacturers is the data source that covers the most RU configurations (from RFUs to AAUs). However, it only provides the total quantity of PCBAs in each RU, and not their breakdown into the four parts which we consider. In parallel, we have PCBA breakdowns between these parts for our own teardown and the 15 external teardowns. We therefore start by establishing a link between the surfaces of these four PCBA parts on the basis of the 16 available teardowns, and then fix certain degrees of freedom of the model to be fitted on the total PCBA surface area of all the 100+ RU configurations available. Figure 16(a) shows that, per TX or RX chain, the PCBA area of the processing units corresponds to around 80% of the PCBA area of the TRXs, while Figure 16(b) shows that the PCBA area of one PA (for one TX chain) corresponds to around 120% of the PCBA area per TX or RX chain of the TRXs. On the other hand, contrary to what we might have expected, we find that the variation in PCBA area for the power supply is not explained by the total power of the RU, represented in Figure 16(c) by the TX power over the whole cell P_{TX}^{cell}. We assume this is due to the same standard voltage of -48 V that supplies all BS components, and hence RUs whatever their configuration.

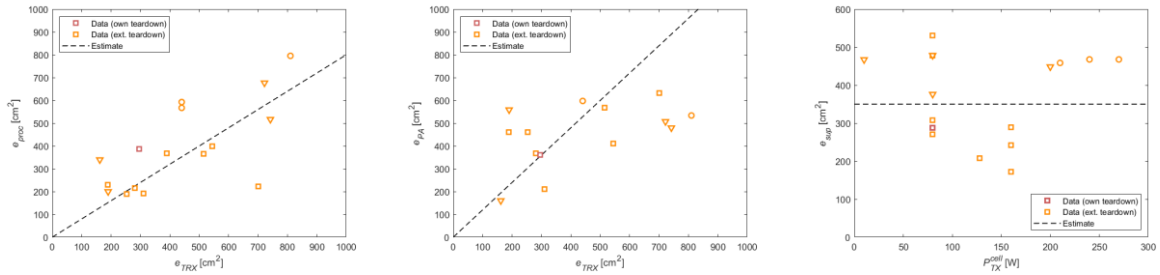

(a) (b) (c)

Fig. 16 Estimates of (a) the ratio of PCBA area for processing units compared to TRX area, (b) the ratio of PCBA area for PAs compared to TRX area, and (c) the PCBA area for the power supply

Table 4 provides the parametric model of RU production and Figure 17 shows related regression analysis. The PCBA areas of a single PA, a single TX (resp. RX) chain, and the processing unit of one TX (resp. RX) chain scale with the maximum output power per TX chain P_{TX}, which is a proxy for their complexity and associated power supply, and hence their size. Next, the scaled PCBA areas are multiplied by the corresponding number of sub-components. Besides, we model the PCBA area dedicated to the power supply as being constant whatever the RU configuration, roughly around 350 cm² (see Figure 17(a) and Figure 17(b)). As an example, let's take a traditional macro-RU with 2 TX and 2 RX chains (i.e., 2T2R), with an output power of 40 W per TRX. According to the parametric model, it would embed a total PCBA area of $350 + (2 + 2) \cdot 51 + (2 + 2) \cdot 63 + 2 \cdot 76 = 958$ cm². Our own teardown for an equivalent RU returned a value of 1330 cm² for the total PCBA area.

The mechanical structure of the RU forms its casing and supports the cavity filters. For RRUs and AAUs installed outdoors, this structure also contributes to passive cooling through heatsinks, while for RFUs installed within the BS cabinet, cooling is assumed to be provided by PSU cooling systems. The mechanical structure is modeled through its mass m_{RU} which scales with the square root of the total PCBA area in the RU, denoted by e_{RU} (see Figure 17(c)). In fact, the mass of the RU structure depends on its dimensions, which in turn mainly depends on the total PCBA area. If the increase in PCBA area were taking place in a single plane, the scaling would be linear. However, manufacturers use spatial arrangements of PCBAs in order to make the RU more compact, explaining the sub-linear scaling.

Finally, we might expect that the recent trend of combining AFEs and PAs from several frequency bands in single platforms to form multi-band RUs will significantly reduce the quantities of electronic and mechanical sub-component thanks to mutualization. However, when allocating these quantities per band of multi-band RUs and comparing them with corresponding quantities of single-band RUs, we cannot find any significant difference. Hence, we rather explain this approach as a cost-cutting strategy, and to facilitate on-site RU installation and dismantling by operators. Therefore, we consider that the proposed parametric model applies to both single-band and multi-band RUs, with each cell modeled individually.

Table 4 Parametric model of RU production

Foreground process type	Parametric functions of foreground process quantities	Numerical estimates of model parameters
Electronic sub-components	$E_{RU} = [e_{sup} \quad e_{proc} \quad e_{TRX} \quad e_{PA}]$ $e_{sup} = e_{sup}^{ref}$ $e_{proc} = (N_{TX} + N_{RX}) \cdot e_{proc}^{ref} \cdot \left(\frac{P_{TX}}{P^{\star}}\right)^{\alpha_{proc}}$ $e_{TRX} = (N_{TX} + N_{RX}) \cdot e_{TRX}^{ref} \cdot \left(\frac{P_{TX}}{P^{\star}}\right)^{\alpha_{TRX}}$ $e_{PA} = N_{TX} e_{PA}^{ref} \cdot \left(\frac{P_{TX}}{P^{\star}}\right)^{\alpha_{PA}}$ $e_{RU} = e_{sup} + e_{proc} + e_{TRX} + e_{PA}$	$e_{sup}^{ref} = 350$ cm² $e_{proc}^{ref} = 8$ cm² $e_{TRX}^{ref} = 10$ cm² $e_{PA}^{ref} = 12$ cm² $\alpha_{proc} = 0.5$ $\alpha_{TRX} = 0.5$ $\alpha_{PA} = 0.5$
Mechanical sub-components	$M_{RU} = [m_{RU}]$ $m_{RU} = m_{RU}^{ref} \cdot \left(\frac{e_{RU}}{A^{\star}}\right)^{\alpha_{RU}}$	$m_{RU}^{ref} = 0.35$ kg $\alpha_{RU} = 0.5$
Upstream transport	$T_{RU} = [t_{RU}]$ $t_{RU} = d_{up} \cdot (e_{RU} \rho_{PCBA} + m_{RU})$	$d_{up} = 1000$ km $\rho_{PCBA} = 0.001$ kg/cm²
Component assembly	$A_{RU} = [a_{RU}]$ $a_{RU} = a_{elec}$	$a_{elec} = 1000$ Wh

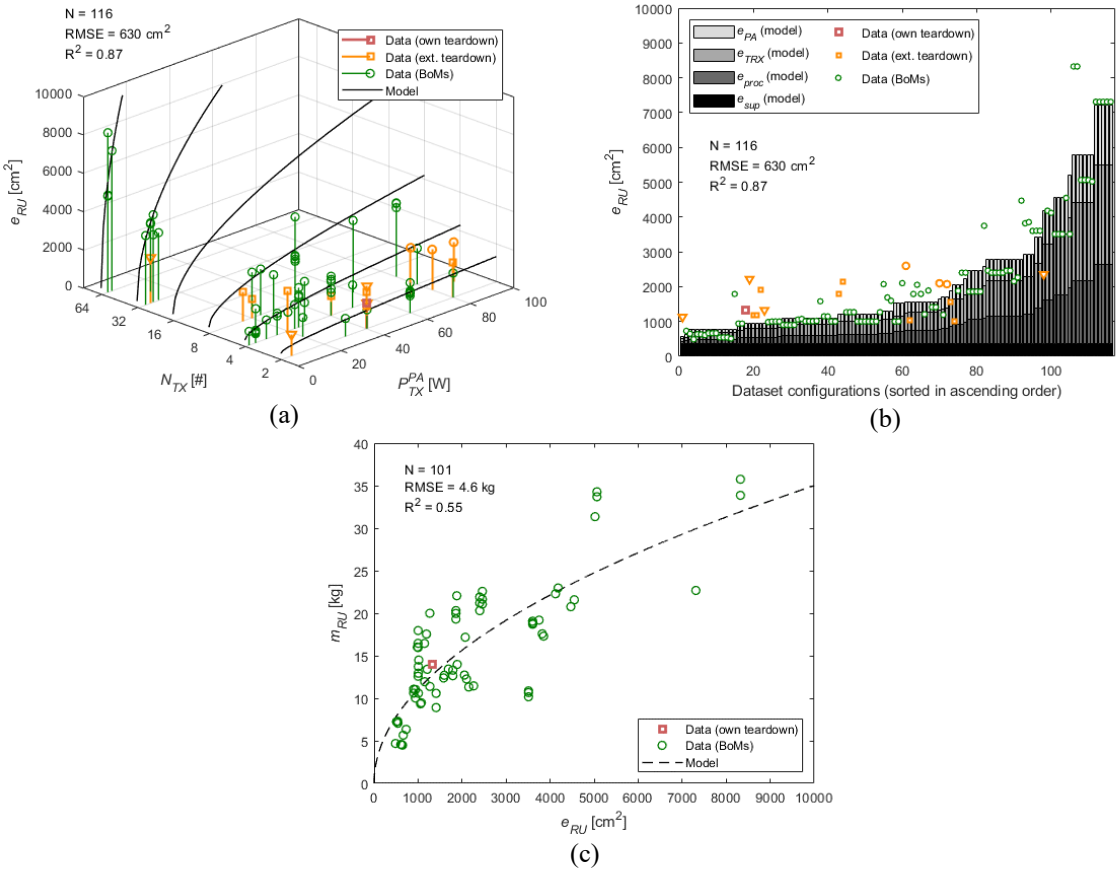

Fig. 17 Regression analysis for the RU production model: (a) total PCBA area vs. key model parameters (i.e., the PA output power and the number of TX chains), (b) breakdown of total PCBA area for all RU configurations (sorted), and (c) total mass of mechanical structure vs. the total area of PCBAs in one RU

3.1.5 Antenna unit production

An antenna array contains n_{AE} antenna elements (AEs) arranged in rows and columns and split into several sub-arrays that vertically group together multiple AEs. Given that one AE is made up of two cross-polarized antennas supporting two spatial data layers at ±45°, the number of sub-arrays in one array is equal to $N_{TRX}/2$ as each sub-array is connected to two TRXs. The electronic sub-components of the AU are the AEs that comprise the radiating elements plus internal cables and RF delay lines. The mechanical structure of the AU consists of a reflective plane focusing the radiation pattern of the antenna and supporting the AEs, plus a radome to protect them from outdoor conditions.

The quantity of both sub-component types depends on n_{AE} and on the wavelength, which we express as

$$\lambda = 30\frac{f^\star}{f} \quad [\text{cm}]\,.$$

It then allows us to calculate the surface area of a single antenna array by multiplying its number of AEs with the antenna area per AE as

$$\mathcal{A}_{array} = n_{AE}\delta_h\delta_v\lambda^2 \quad [\text{cm}^2]\,,$$

where δ_v and δ_h are the vertical and horizontal spacings between AEs, expressed in wavelength multipliers. These spacings influence how the RF signals combine with each other in far field (Delos et al. 2020). In this work, δ_h is estimated to be 0.5 with ABF and 0.7 without ABF, and the vertical spacing δ_v is 0.7 in both case, which is a good trade-off between a narrower beam width and greater side-lobes (Tahseen et al. 2023).

For calculating n_{AE}, we decompose the maximum total antenna gain into a product of the AE gain G_{AE}, the array gain of the sub-array (namely the sub-array factor) G_{SF}, and the maximum beamforming gain G_{BF}, as

$$G_{TX} = G_{AE}G_{SF}G_{BF} \quad [/]\,.$$

This product becomes a sum when the gains are expressed in decibel scale:

$$G_{TX,dBi} = G_{AE,dBi} + G_{SF,dB} + G_{BF,dB} \quad [\text{dBi}]\,.$$

With ABF, G_{BF} is equal to the number of sub-arrays in the antenna array, otherwise it equals to 1. In a vertical linear sub-array, G_{SF} equals to the number of AEs, hence the number of sub-array rows. When this information is not available in the technical documentation, we estimate the sub-array gain as in Delos et al. (2020):

$$G_{SF} = \frac{0.886}{\psi_{vHPBW}\delta_v\cos(\psi_{tilt})} \quad [/]\,,$$

where ψ_{vHPBW} is the vertical HPBW angle and ψ_{tilt} is the down-tilt angle of the antenna beam, both expressed in radians (see Figure 18(a)). Then, knowing G_{SF}, G_{BF} and G_{TX} for all AU configurations in our data sources, we estimate that G_{AE} equals to 7 dBi without ABF and 5 dBi with ABF (see Figure 18(b)). This difference is explained by the reflectors that are added behind the AEs in traditional AUs without ABF to further focus the single beam in the horizontal plane. Yet, these reflectors are not used with ABF because they are detrimental to the azimuthal signal combination (which enables beam formation), even if the AE gain is slightly degraded.

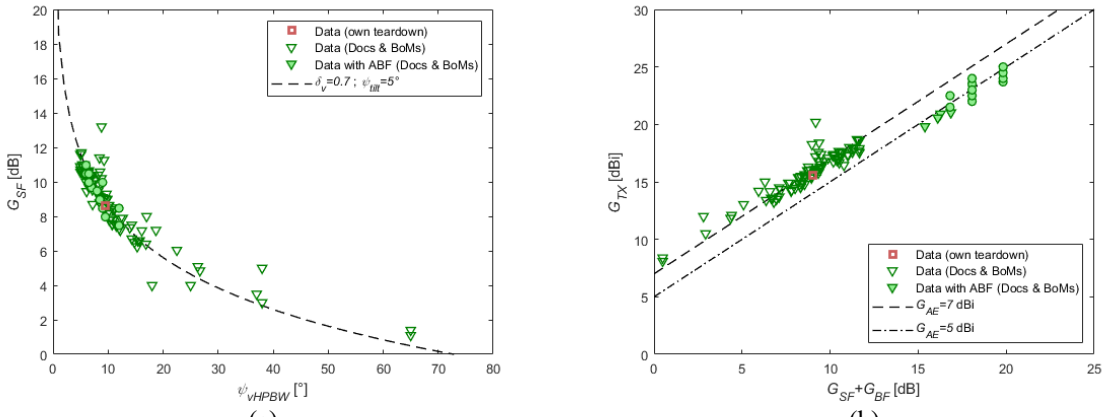

Fig. 18 Antenna gain analysis: (a) sub-array gain vs. vertical HPBW of the sub-array, and (b) maximum total antenna gain vs. sub-array plus beamforming gain for estimating the gain of AEs in AU without and with ABF

Table 5 provides the parametric model of AU production and Figure 19 shows related regression analysis. The size of one AE linearly scales with the wavelength of the RF signal it emits. Since a higher carrier frequency results in a smaller wavelength, we scale its mass with the inverse of f yielding $\alpha_{AE} = -1$ (see Figure 19(a)). Next, we distinguish between two cases to compute the total mass of all AEs, denoted e_{AE}. First, without ABF, $G_{BF} = 1$ and each sub-array handles a specific spatial data layer, meaning that the maximum total antenna gain is equal to the total gain of one sub-array. The number of AEs per sub-array is calculated as G_{TX}/G_{AE} and the number of sub-arrays corresponds to $N_L/2$ as each sub-array transmits two layers thanks to cross-polarization. We then multiply the number of AEs per sub-array by the number of sub-arrays to obtain n_{AE}. Second, with ABF, all sub-arrays transmit all spatial data layers (that are precoded) and participate in beamforming such that $G_{BF} = N_{TRX}/2$. In that case, the number of AEs is directly $n_{AE} = G_{SF}G_{BF}$. Let's take the example of an 8-layer cell with an antenna gain of 17 dBi: without ABF, a traditional 8T8R AU with 32 AEs is needed, whereas with an AAU, 16 AEs are sufficient, at least in 8T8R, and up to 32T32R depending on the desired beamforming adaptivity degree.

For calculating the mass of AU structure, we first need to calculate surface area of antenna arrays as in Figure 19(b). Then, we again distinguish between two cases: (i) the traditional "passive" AU physically separated from the RU, and (ii) the so-called "active" AU integrated with the RU in an AAU. In a traditional AU, antenna arrays of different frequency ranges, as defined by the standard AISG (2018), can be superimposed in order to save space and reduce the wind load, e.g., the low-frequency range between 0.5 and 1 GHz and the mid-frequency range between 1.5 and 2.4 GHz. This means that antenna arrays at, e.g., 0.8 and 1.8 GHz can be superimposed, but not those at 1.8 and 2.1 GHz. The area occupied by a given frequency range j is the sum of all its $N_{B,j}$ antenna array areas, denoted by $\mathcal{A}_{array,i}$ for a frequency band i. The total mass of mechanical structure in a complete AU scales linearly with the total antenna area (see Figure 19(c)), which corresponds to the greatest area occupied by one frequency range. To compute m_{AU}, the mass of mechanical structure for one cell, the total mass of the AU is uniformly allocated per supported band. The case of active AU is simpler because a single AAU supports only one frequency band. The calculation of the antenna area is the same as for traditional AUs, but here no mass allocation between cells is needed.

Table 5 Parametric model of AU production

Foreground process type	Parametric functions of foreground process quantities	Numerical estimates of model parameters
Electronic sub-components	$E_{AE} = [e_{AE}]$ $e_{AE} = n_{AE} e_{AE}^{ref} \cdot \left(\frac{f}{f^\star}\right)^{\alpha_{AE}}$ without ABF: $n_{AE} = \frac{G_{TX}}{G_{AE}} \frac{N_L}{2}$ with ABF: $n_{AE} = \frac{G_{TX}}{G_{AE}}$	$G_{AE} = 7 \mid 5$ (ABF) dBi $e_{AE}^{ref} = 0.3$ kg $\alpha_{AE} = -1$

Mechanical sub-components	$M_{AU} = [m_{AU}]$
	$\mathcal{A}_{array} = n_{AE}\delta_h\delta_v \cdot \left(30\frac{f^\star}{f}\right)^2$
	if traditional AU:
	$\mathcal{A}_{AU} = \max_j \left(\sum_{i=1}^{N_{B,j}} \mathcal{A}_{array,i}\right)$
	$m_{AU} = \frac{1}{\sum N_{B,j}} m_{AU}^{ref} \cdot \left(\frac{\mathcal{A}_{AU}}{\mathcal{A}^\star}\right)^{\alpha_{AU}}$
	else if AAU:
	$m_{AU} = m_{AU}^{ref} \cdot \left(\frac{\mathcal{A}_{array}}{\mathcal{A}^\star}\right)^{\alpha_{AU}}$
		$\delta_v = 0.7$
		$\delta_h = 0.7 \mid 0.5$ (ABF)
		$m_{AU}^{ref} = 0.004 \mid 0.001$ (AAU) kg
		$\alpha_{AU} = 1$

Upstream transport	$T_{AU} = [t_{AU}]$ $t_{AU} = d_{up} \cdot (e_{AE} + m_{AU})$	$d_{up} = 1000$ km
Component assembly	$A_{AU} = [a_{AU}]$ $a_{AU} = a_{elec}$	$a_{elec} = 1000$ Wh

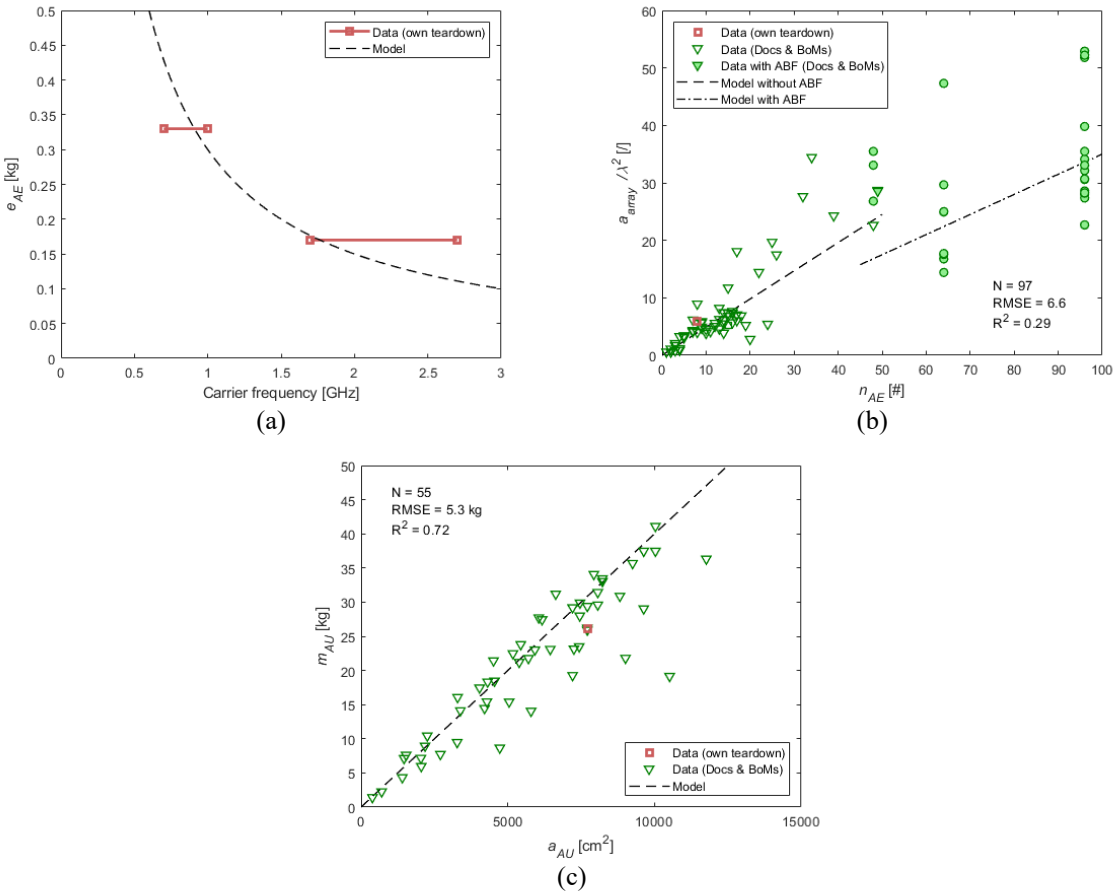

Fig. 19 Regression analysis for the AU production model: (a) mass of AEs vs. carrier frequency, (b) normalized area of the antenna array vs. the number of AEs in the array, without and with adaptive beamforming, and (c) total mass of mechanical structure vs. the total antenna area in one AU

3.1.6 Power supply unit production

The size of the PSU required for an entire BS, and hence the quantity of its sub-components, primarily depends on p_{supply}, the total supply power required by the BS. This value is the maximum achievable value of p_{cons}, the total power consumption of the BS which varies during the day. The way to calculate p_{cons} is explained in the modeling of the use stage module. Table 6 provides the parametric model of PSU production and Figure 20 shows related regression analysis.

We consider two electronic sub-components for the PSU: the power converter (for AC/DC conversion) and the backup batteries, both modeled by their mass, denoted e_{conv} and e_{batt} respectively. The power converter consists mainly of rectifiers, plus a power distribution panel, a controller and fans for active cooling. The mass of the power converter scales linearly with p_{supply} (see Figure 20(a)) plus an additional power supply margin δ_{marg} that takes into account PSU losses (with typical efficiency of over 95%) and other system robustness aspects. Based on the technical documentation, we assume a typical power supply margin of 25%. The mass of backup batteries varies with the desired energy storage denoted ϵ_{back} (see Figure 20(b)), which is expressed as the product of p_{supply} and τ_{back}, the backup duration at full BS load. Of course, the actual backup duration may be longer than τ_{back} as the BS does not operate at full load all the time. Furthermore, we might expect the BS to go into safety mode in case of supply failure, reducing its power consumption by deactivating part of its bands (e.g., the high-frequency capacity bands) in order to guarantee a basic service. This way, the backup batteries can last even longer. The mechanical structure of the PSU consists of the sub-rack that houses the electronic sub-components plus the BS cabinet. The total mass of this structure, denoted m_{PSU}, scales linearly with the total mass of electronics denoted by e_{PSU} (see Figure 20(c)).

Table 6 Parametric model of PSU production

Foreground process type	Parametric functions of foreground process quantities	Numerical estimates of model parameters
Electronic sub-components	$E_{PSU} = [e_{conv} \quad e_{batt}]$ $p_{supply} = \max(p_{cons})$ $e_{conv} = e_{conv}^{ref} \cdot \left(\frac{p_{supply}}{P^\star} \cdot \left(1 + \delta_{marg}\right)\right)^{\alpha_{conv}}$ $e_{batt} = e_{batt}^{ref} \cdot \left(\frac{p_{supply}}{P^\star} \cdot \frac{\tau_{back}}{\tau^\star}\right)^{\alpha_{batt}}$ $e_{PSU} = e_{conv} + e_{batt}$	$\delta_{marg} = 0.25$ $e_{conv}^{ref} = 0.001$ kg $e_{batt}^{ref} = 0.9$ kg $\alpha_{conv} = 1$ $\alpha_{batt} = 0.5$
Mechanical sub-components	$M_{PSU} = [m_{PSU}]$ $m_{PSU} = m_{PSU}^{ref} \cdot \left(\frac{e_{conv}}{\mathcal{M}^\star}\right)^{\alpha_{PSU}}$	$m_{PSU}^{ref} = 2.3$ kg $\alpha_{PSU} = 1$
Upstream transport	$T_{PSU} = [t_{PSU}]$ $t_{PSU} = d_{up} \cdot (e_{PSU} + m_{PSU})$	$d_{up} = 1000$ km
Component assembly	$A_{PSU} = [a_{PSU}]$ $a_{PSU} = a_{elec}$	$a_{elec} = 1000$ Wh

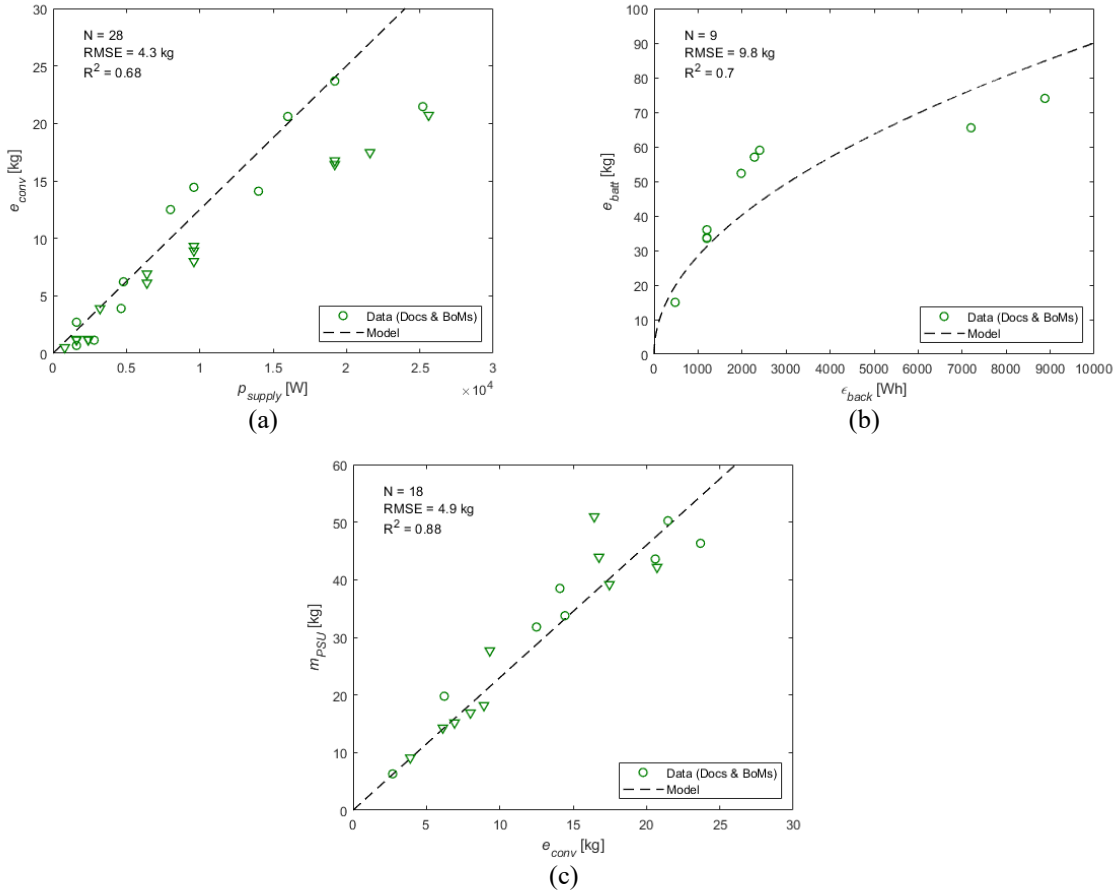

Fig. 20 Regression analysis for the PSU production model: (a) mass of the power converter vs. the total supply power required by the BS, (b) mass of the backup battery pack vs. its energy storage capacity, and (c) mass of the PSU structure vs. the mass of power converters

3.1.7 Cable production

Table 7 provides the parametric model of cable production. No model parameters need to be estimated for this LCA module. The quantities of data cables for one cell are modeled by their length, denoted by e_{opt} and e_{coax} for optical fibers and coaxial cables respectively, which depend on d_{AU}, the distance between the BBU and the AUs. For a tower-mounted BS, this distance is typically the height of the tower, e.g., about twenty meters. Other configurations are possible, e.g., when the BS is installed on top of an existing building. Next, the relative RU position between the BBU and the AU, such that $0 < \delta_{cab} \leq 1$, defines the share or total length between optical and coaxial cables. For instance, an RFU installed in the same cabinet as the BBU implies that δ_{cab} is close to 0, whereas an RRU installed close to the AU implies that δ_{cab} is closer to 1. Since AAUs integrate the AU and the RU in the same unit, coaxial cables are not needed and $\delta_{cab} = 1$. We assume that a single optical fiber is enough for one cell since it supports a data rate of around 10 Gbps, while the number of parallel coaxial cables is the same as the number of TRX in the RU, thus the number of antenna sub-arrays. The length of power cables feeding the RUs is denoted e_{pwr} and is assumed to be equal to that of optical fibers. For the distribution and the end-of-life stages modules, the masses of the three types of cable can be calculated using their linear density given by ρ_{opt}, ρ_{coax} and ρ_{pwr}, that we estimate to be $\rho_{opt} = 0.004$ kg/m, $\rho_{coax} = 0.090$ kg/m and $\rho_{pwr} = 0.160$ kg/m, respectively.

Table 7 Parametric model of cable production

Foreground process type	Parametric functions of foreground process quantities	Numerical estimates of model parameters
Electronic sub-components	$E_{cab} = [e_{opt} \quad e_{coax} \quad e_{pwr}]$ $e_{opt} = d_{AU}\delta_{cab}$ $e_{coax} = N_{TRX}d_{AU} \cdot (1 - \delta_{cab})$ $e_{pwr} = d_{AU}\delta_{cab}$	/
Mechanical sub-components	n.a.	n.a.
Upstream transport	n.a.	n.a.
Component assembly	n.a.	n.a.

3.2 Distribution stage module

The distribution stage includes the transport of BS components from their final assembly facility to the specific site where the BS operates, plus the installation of these components on site. Table 8 provides the parametric model of the distribution stage and Figure 21 shows the related regression analysis.

The international transport is modeled by a mix of freight transportation means for a given mass over a given distance, as for the upstream transport of sub-components. The mass of each component is calculated by summing the mass of its electronic and mechanical sub-components, using the same mass densities as before if the sub-component quantity is not expressed in kg. On top of this, we add the mass $m_{pack}(x)$ of the specific packaging, that we no longer consider negligible for worldwide freight, and that we model by an average mass overhead δ_{pack} estimated to be about 30%. The international transport distance d_{inter} depends on where the BS components are manufactured and where the operator is based. The total international freight (in kg·km) for the entire BS is the sum of the freight for its N_{comp} components.

The local transport is dedicated to the installation of the BS and is handled by a small truck, whose all impacts are allocated to the BS (and no longer allocated with respect to the transported mass, as for international freight). Therefore, we simply model it by d_{loc} which corresponds to the round-trip distance between the operator's warehouse and the BS site location.

The installation of BS components on site consists of manual handling, assembly of mechanical parts, cable connections and system configuration, all carried out by one or more technicians. Due to a lack of primary data, we assume the same electricity consumption for the installation, denoted by a_{inst}, as for the assembly of BS components, i.e., 1000 Wh, with a wide range of uncertainty. We consider that the technicians travel in the same truck as the BS components.

Altogether, the row vector of process quantities for the distribution stage module is

$$Q_{dist}(x) = [m_{pack}(x) \quad t_{inter}(x) \quad t_{loc} \quad a_{inst}] .$$

Table 8 Parametric model of the distribution stage

Foreground process	Parametric functions of foreground process quantities	Numerical estimates of model parameters
Packaging	$m_{comp,i}(x) = \sum_{k=1}^{\widetilde{K}_i} q_{k,i}(x)\rho_{k,i}$ $m_{pack,i}(x) = m_{comp,i}(x)\delta_{pack}$ $m_{pack}(x) = \sum_{i=1}^{N_{comp}} m_{pack,i}(x)$	$\rho_{PCBA} = 0.001$ kg/cm² $\rho_{opt} = 0.004$ kg/m $\rho_{coax} = 0.090$ kg/m $\rho_{pwr} = 0.160$ kg/m $\delta_{pack} = 0.3$ kg
International transport	$t_{inter}(x) = d_{inter} \cdot \left(m_{pack}(x) + \sum_{i=1}^{N_{comp}} m_{comp,i}(x)\right)$ $t_{loc} = d_{loc}$	/
Installation	$a_{inst} = a_{elec}$	$a_{elec} = 1000$ Wh

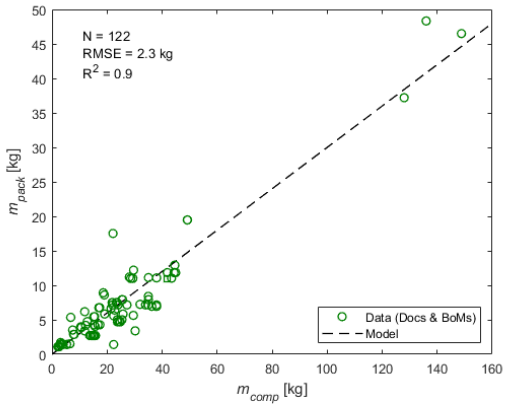

Fig. 21 Mass of the packaging vs. mass of the component

3.3 Use stage module

The use stage of the BS consists solely of electricity consumption since support activities, e.g., maintenance, are excluded from the scope of the model. Various electricity sources can be used to supply the BS, and the model allow to choose between three typical ones: the electricity grid, a diesel generator, or a PV system. The energy consumption of all BS components is computed as the integral of the BS power consumption $p_{cons}(x,t)$ over its lifetime L as

$$Q_{use}(x) = \varepsilon_{cons}(x) = \int_0^L p_{cons}(x,t)\mathrm{d}t \quad [\mathrm{Wh}] .$$

In this work, we reuse the parametric power model proposed by Golard et al. (2024) to model $p_{cons}(x,t)$. They propose two versions of their BS power model: (i) an instantaneous model at the scale of hundred µs, and (ii) an average model at the scale of one hour. For life-cycle modeling, the hourly time scale is appropriate, and we therefore suggest using the average power model allowing to compute the average BS power consumption on an hourly basis, denoted $\bar{p}_{cons}\left(x, \bar{l}(t)\right)$ where $\bar{l}(t)$ is the average hourly BS load. With H the total number of hours in the BS lifetime, the BS energy consumption can be rewritten as

$$\varepsilon_{cons}(x) = \sum_{h=1}^{H} \bar{p}_{cons}\left(x, \bar{l}(h)\right) \quad [\mathrm{Wh}] .$$

Finally, if the average BS power model is linear (which is the case without power-saving features such as sleep modes), we can simplify the previous equation as

$$\varepsilon_{cons}(x) = L \cdot 365 \cdot 24 \cdot \bar{p}_{cons}(x, \bar{l}_{avg}) \quad \text{[Wh]}\,,$$

where $\bar{l}_{avg}$ is the average BS load in terms of physical resources over its whole lifetime. The complete BS power model is provided in Golard et al. (2024) with all numerical parameters.

Some terminology differences should be noted between this work and Golard et al. (2024). First, in this work, the BS components represent physical BS components, whereas Golard et al. (2024) consider BS sub-parts providing specific functions: e.g., we consider that the RU is a single BS component, whereas Golard et al. (2024) consider the AFE and the PA to be two different functional blocks because they provide different functions in the RU. Nevertheless, the described physical implementation of their functional blocks is consistent with our life-cycle model and, which validates the use of their power model in this work. Second, they denote the maximum PA output power as P_{TX}^{max} and the load as $x(t)$, which in this work we denote as P_{TX} and $l(t)$. Third, as the AU and cables do not consume energy as such, these components are not taken into account by Golard et al. (2024). Therefore, they do not use model variables such as G_{TX} and δ_{cab}.

3.4 End-of-life stage module

Table 9 provides the parametric model of the end-of-life stage. No model parameters need to be estimated for this LCA module. The electricity consumption for de-installation is modeled as the installation such that $a_{deinst} = a_{inst}$, and the local collection as the local distribution such that $t_{col} = t_{loc}$. The disassembly of all BS components into electronic and mechanical sub-components is modeled as the counterpart to the assembly of all BS components by summing a_{BBU}, a_{RU}, a_{AU} and a_{PSU} for all components of the entire BS. Yet, in this case, the local electricity grid mix is used rather than the electricity mix used for the final assembly. Waste management is assumed to take place in the same region as the BS use, meaning that no international transport is required, but downstream transport is considered, denoted $t_{down}(x)$, which is modeled like upstream transport. The impacts of waste management routes are assumed to be proportional to the mass of electronic and mechanical sub-components, denoted $e_{waste}(x)$ and $m_{waste}(x)$ respectively. We denote by $\tilde{K}_{elec,i}$ and $\tilde{K}_{mech,i}$ the number of respectively the electronic and mechanical sub-components in a BS component i.

The complete row vector of process quantities for the end-of-life stage module is

$$Q_{EoL}(x) = [a_{deinst} \quad t_{col} \quad a_{disas}(x) \quad t_{down}(x) \quad e_{waste}(x) \quad m_{waste}(x)]\,.$$

Table 9 Parametric model of the end-of-life stage

Foreground process	Parametric functions of foreground process quantities	Numerical estimates of model parameters
Waste management of sub-components	$e_{waste}(x) = \sum_{i=1}^{N_{comp}} \sum_{k=1}^{\tilde{K}_{elec,i}} q_{k,i}(x)\rho_{k,i}$ $m_{waste}(x) = \sum_{i=1}^{N_{comp}} \sum_{k=1}^{\tilde{K}_{mech,i}} q_{k,i}(x)\rho_{k,i}$	$\rho_{PCBA} = 0.001$ kg/cm² $\rho_{opt} = 0.004$ kg/m $\rho_{coax} = 0.090$ kg/m $\rho_{pwr} = 0.160$ kg/m
Local collection and downstream transport	$t_{col} = d_{loc}$ $t_{down}(x) = d_{up} \cdot (e_{waste}(x) + m_{waste}(x))$	$d_{up} = 1000$ km
De-installation and disassembly	$a_{deinst} = a_{elec}$ $a_{disas}(x) = a_{elec} \cdot (1 + 3N_C)$	$a_{elec} = 1000$ Wh

4 IAF calculations

This section details how we build background processes to calculate impact assessment factors (IAFs). This section covers the production stage only, which is the primary focus of our model. We first explain the custom unit processes developed in this work for certain electronic parts. We also discuss the reasons for proposing these custom unit processes, how the data sources are used, and how these custom processes compare to original ecoinvent unit processes. Second, we explain how we use the data sources to estimate the composition of electronic and mechanical sub-components of the model. The complete inventories of unit processes used to build all the background processes of the BS model are provided in Online Resource 2.

4.1 Custom unit processes for electronic sub-components

This section describes the custom unit processes developed in the context of this work. These custom unit processes are differentiated from the original ecoinvent unit processes thanks to a "(custom UCLouvain)" mention in their name. The main data sources for developing these custom unit processes are the versions of these unit processes in ecoinvent (when they exist) and full material declarations (FMDs) of specific components from manufacturers (referred to as bill-of-material in the paper). A FMD discloses, for a component, the mass distribution between its different homogeneous materials and the composition of these homogenous materials (i.e., the mass of casing and pins in an electrical connector and the material composition of this casing and these pins). In the following, we list all the "(custom UCLouvain)" unit processes. We detail the reason we modeled these custom unit processes, the data sources we used, and we discuss the results obtained and key differences.

4.1.1 Integrated circuits

Process names: "*market for integrated circuit, logic type*" & "*market for integrated circuit, memory type*"

The reasons we propose custom unit processes for integrated circuits (ICs) are:

- Pirson et al. (2022) highlighted a potential overestimation of the GWP of the production of ICs in the ecoinvent database. As ICs are identified as an environmental hot spot in our work, we challenged and modified the ecoinvent assumptions contributing the most to their GWPs.
- We consider that the reference flow in "cm² of die" for the IC is more appropriate than the current reference flow in "kg of packaged IC" as most of the environmental impact of the production of ICs occur during the production of the die itself (Boyd 2011, Pirson et al. 2022).

Therefore, we propose the following modifications (summarized in Figure 22).

(1) The change of the reference flow from "kg of packaged IC" to "cm² of die". This is a methodological choice that allows us to model ICs with respect to their die area. It also simplifies the implementation of the following modifications. To comply with the reference flow in "cm² of die", we consider that 1 kg of IC contains 175 cm² of die (Wattiez et al. 2024).
(2) A change of the gold mass contained in IC packages. Gold is used in some type of wire bonding technologies to connect the die to the pins of the package. Based on 62 IC FMDs from various manufacturers, we performed linear regression analysis to estimate an average mass of gold per kg of packaged IC. We used 56 and 6 FMDs for IC logic type and IC memory type respectively. Figure 23 shows the raw data and the results of the regression analysis, which are 2.2 and 2.1 g of gold per kg of IC logic and IC memory respectively. The original ecoinvent unit processes assume 10.3 g and 1 g per kg of IC logic and IC memory respectively. We then scale the mass of gold per cm² of die rather than per kg of packaged IC.
(3) A reduction of the electricity used during the dicing and packaging step. Pirson et al. (2022) highlighted two sources assessing this quantity: (i) the study from William et al. (2002), which is currently used by ecoinvent, estimating the electricity consumption of 0.34 kWh per cm² of die, and (ii) a more recent study from Prakash et al. (2013) mentioning industry estimating the electricity consumption at 0.55 kWh per cm² of die. In this work, we use estimates from William et al. (2002).
(4) The amount of processed wafer required for 1 cm² of functional die is estimated by considering yields on the wafer manufacturing and packaging processes. Boakes et al. (2023) consider 3 types of yield: (i) a line yield of 90%, (ii) a cut-die yield of 72%, and (iii) a die yield of 86%. The total yield from wafer area to die area is then 56%.
(5) A reduction of the electricity required to produce 1 m² of wafer. The electricity required for the production of the wafer is estimated using data from Boakes et al. (2023) for the production of a wafer using the 28 nm technological node. In their study, they estimate that 686 kWh of electricity is required for a 300 mm wafer resulting in a consumption of 9705 kWh per m² of wafer.
(6) For all other materials and processes, we scale their quantities from the original ecoinvent unit process to the custom one considering that 1 kg of IC models 175 cm² of die (Wattiez et al. 2024).
(7) We apply the same approach as (6) for transportation.

Figure 24 compares the GWP results of original and custom unit processes. It shows a reduction in the relative GWP contributions from gold and packaging electricity for the ICs, and that around 65% of the GWP of the custom IC model is due to the production of the wafer.

Future work related to the proposed modifications are:

(2) Gold mass in ICs should be further studied by collecting more data and differentiating package types.
(3) More up-to-date data should be collected to better understand the energy consumption to cut and package the dies into ICs.
(4) Cut-die yield and die yield depend on the size of the die, as larger dies increase the losses of wafer at the edges and increase the probability of defects for every die (Boakes et al. 2023).
(5) Pirson et al. (2022) and Boakes et al. (2023) highlight the influence of the technological node on the electricity consumption of the wafer fabrication as the processes for more advanced technological nodes require more electricity than for older technologies.
(6) More up-to-date and package differentiated data are needed for a better modeling of other materials and chemicals than gold and electricity consumption.

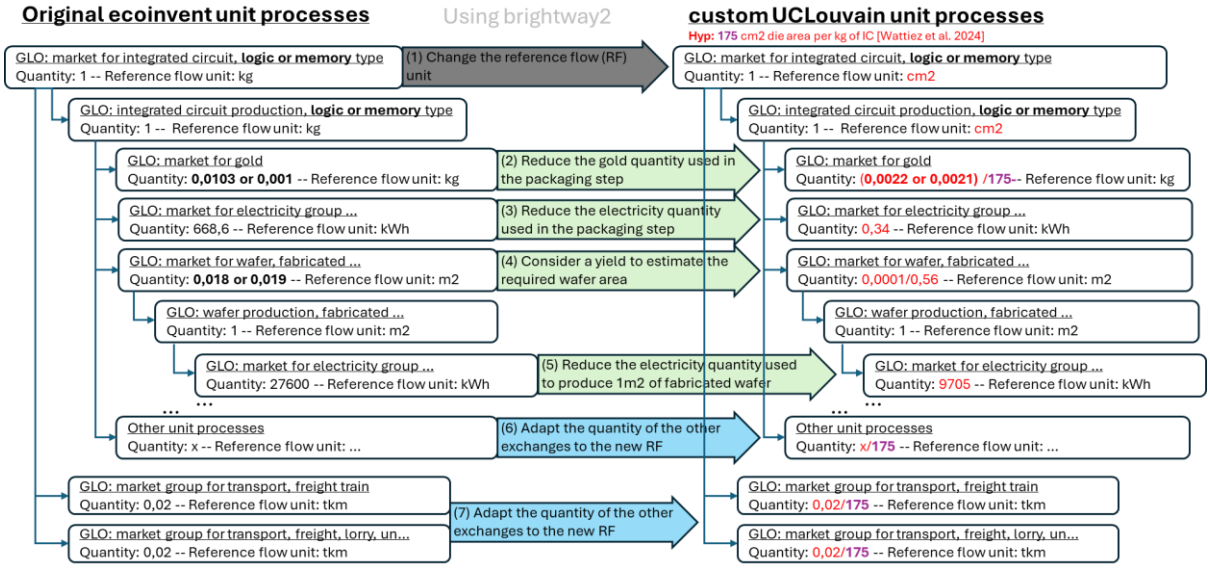

Fig. 22 Structure of the IC logic and IC memory unit processes with the seven modifications of the original ecoinvent IC unit processes (left) to create the "custom UCLouvain" unit processes (right)

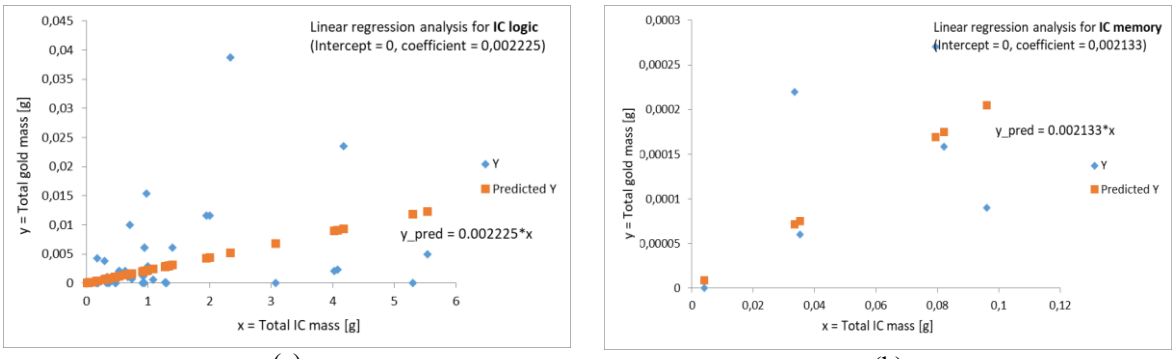

(a) (b)

Fig. 23 Raw data and regression analysis results to estimate the mass of gold with respect to the total mass of IC (a) for IC logic type, and (b) for IC memory type

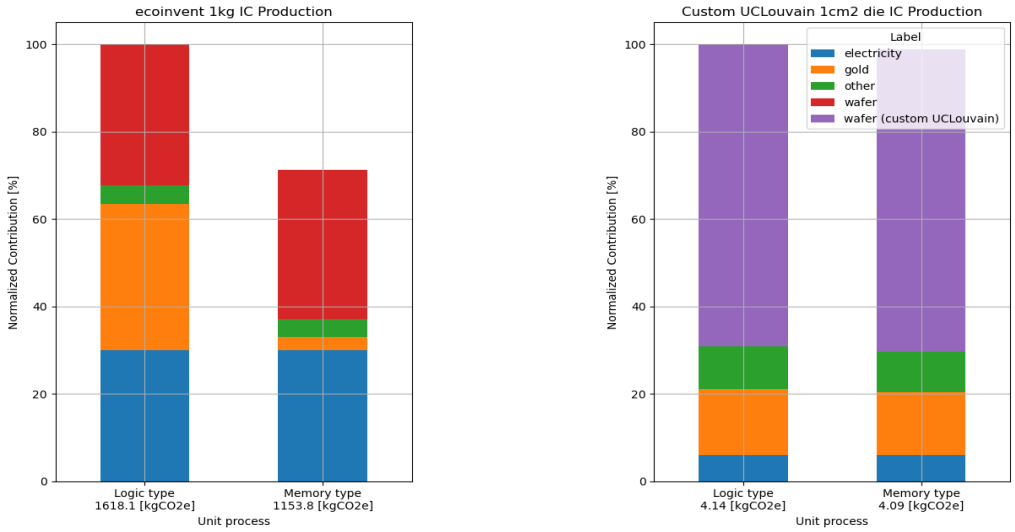

Fig. 24 Comparison of the normalized GWP contributions for the production of both types of integrated circuits (a) for the original ecoinvent unit processes, and (b) for the custom UCLouvain unit processes

4.1.2 Connectors

Process name: "*market for connector, …*"

The reason we propose custom unit processes for connectors is:

- Too few and non-specific connectors are available in ecoinvent.

Therefore, we followed these steps to develop custom unit processes:

- We used teardowns of BS connectors as primary data source (see Figure 25) and combined it with non-specific manufacturer FMDs to estimate average compositions of homogeneous materials (pins and coating for the various types of connectors).
- Due to a lack of data, we considered 6.51 kWh of electricity for the manufacturing processes of 1 kg of connector. This assumption is based on the ecoinvent unit processes "*electric connector production, wire clamp"* and "*electric connector production, peripheral type bus*".

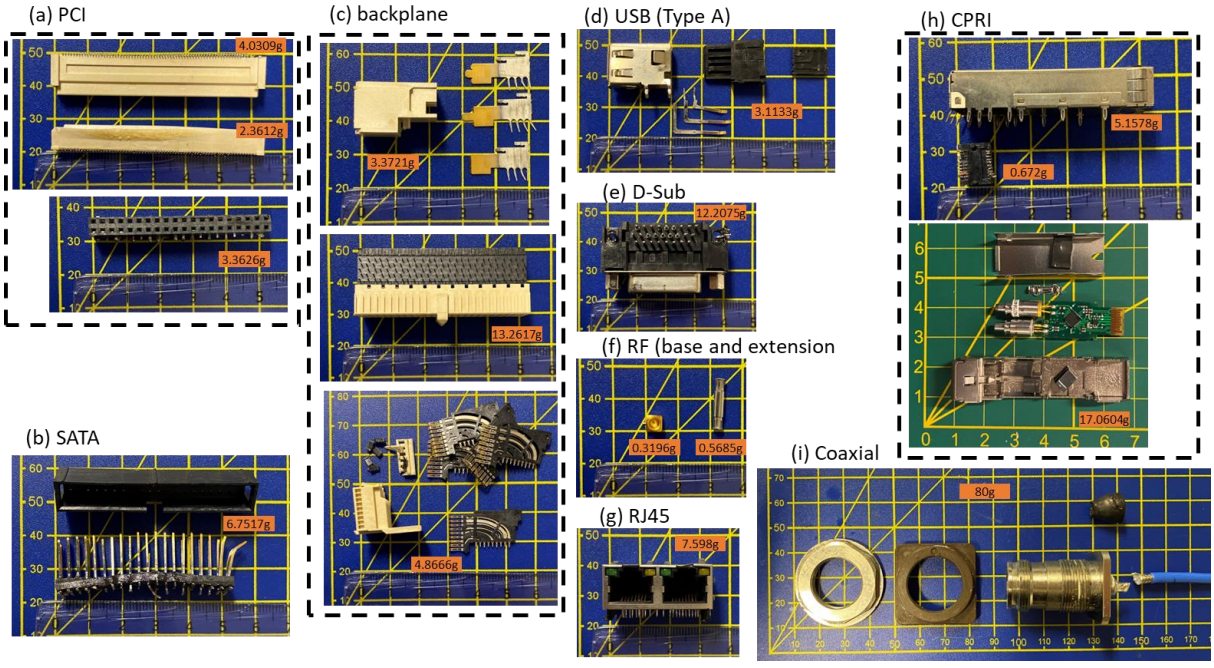

Fig. 25 Picture and masses of connectors categorized in the following connector types: (a) PCI, (b) SATA, (c) backplane, (d) USB, (e) D-Sub, (f) RF, (g) RJ45, (h) CPRI, and (i) coaxial

Figure 26 shows that the use of gold in a connector is never negligible and might contribute the most to the GWP depending on its quantity. After gold, the production of copper and the estimated electricity consumption of the manufacturing processes are two important contributors to the GWP.

Future work should complete the model by considering process losses, specific electricity and heat requirements, other inputs, and direct emissions from the manufacturing processes.

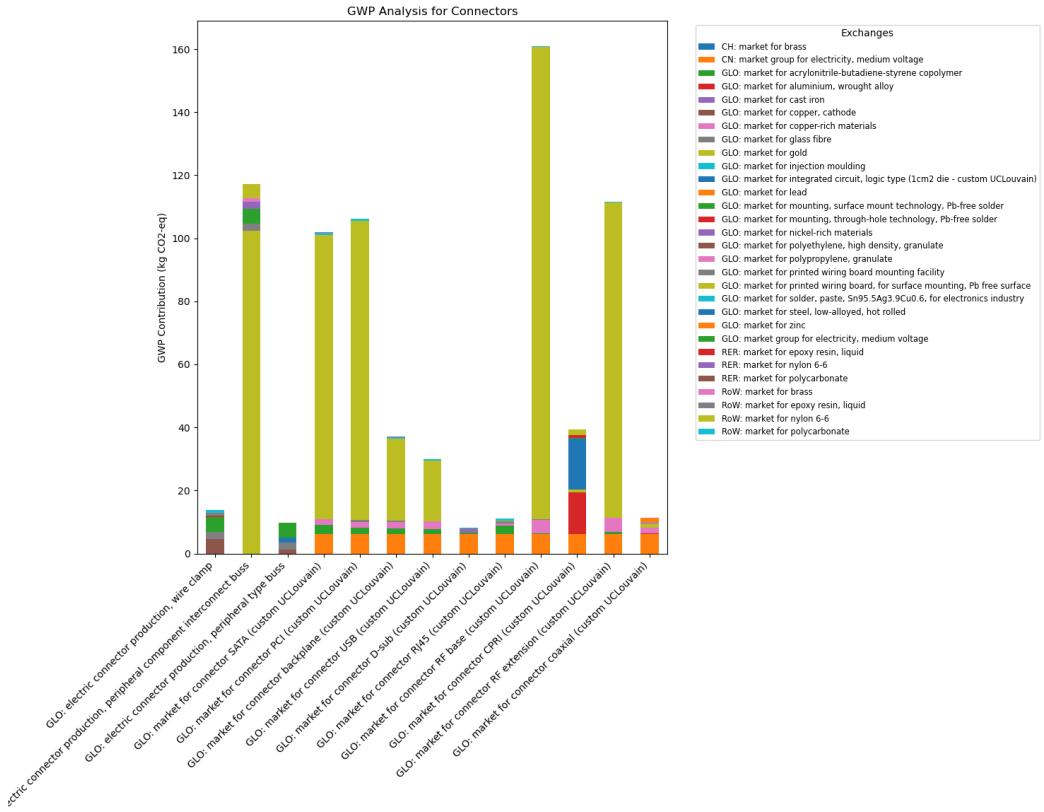

Fig. 26 Comparison of GWP for the production of 1 kg of different types of connectors between the original ecoinvent and custom UCLouvain unit processes

4.1.3 Power amplifiers

Process names: "*market for power amplifier …*" & "*market for RF coupler*"

The reason we propose custom unit processes for power amplifiers is:

- No power amplifier nor RF coupler unit processes are available in ecoinvent.

Therefore, we followed these steps to develop custom unit processes:

- We modeled these components by their constituents that we retrieved from the FMDs provided by the manufacturers. As a first approximation, we included the material that contributed to more than 5% of the total mass, as well as gold and silver. The two power amplifiers are LDMOS transistors characterized by their respective power of 6.3 W (model: NXP AFT20P060-4NR3) and 63 W (model: NXP AFT18H356-24S). Note that the latter features an asymmetrical Doherty design. These power amplifiers are designed for cellular base station applications covering the frequency range of 1805 to 2170 MHz.

Figure 27 shows that the production of gold accounts for about 80% of the GWP of the production of power amplifiers.

Future work should complete the model by considering process losses, specific electricity and heat requirement, other inputs, and direct emissions of the manufacturing processes.

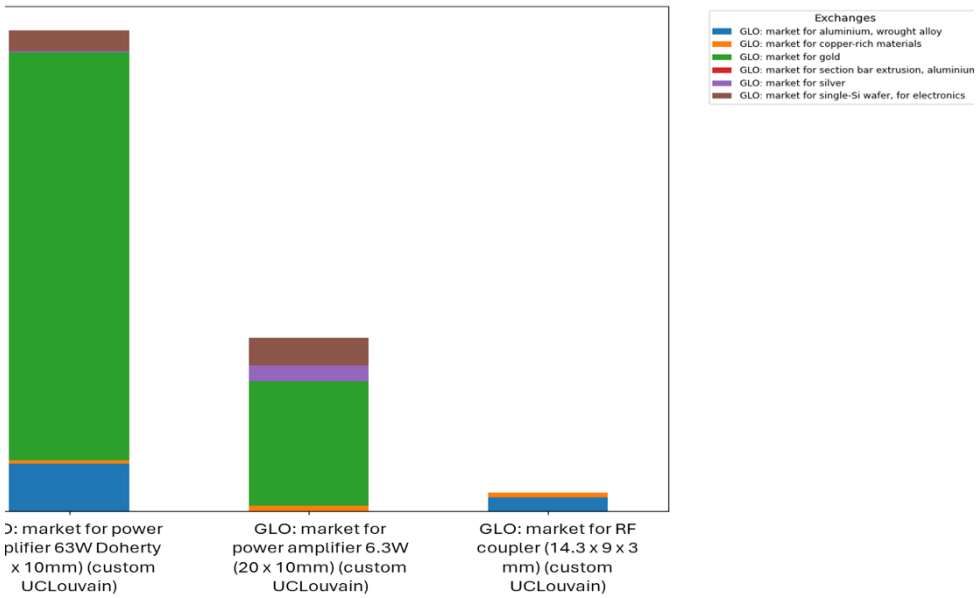

Fig. 27 GWP for the production of PA and RF components for the custom UCLouvain unit processes

4.2 Modeling assumptions for metal and polymer processing

For complete modeling of sub-component manufacturing, the processes that transform raw materials into final products must be considered with their respective losses. In Table 10, we summarize the assumptions for modeling these transformation processes and related losses for metal and polymer parts used in the production of BS components. The specific ecoinvent unit processes are given in Online Resource 2.

Table 10 Processes and related losses for different metal and polymer parts

Material	Processes and related losses
Die-cast aluminum part	Aluminum die-cast blanks are produced using a cast aluminum alloy and a die-casting process (which is not modeled in ecoinvent). Then, to produce the final parts, the die-cast parts are processed by a milling process which we assume to have 5% of losses as in Sphera Managed LCA Content and König et al. (1995).
Aluminum sheet	Aluminum sheets are produced from a wrought aluminum alloy and a sheet rolling process for which ecoinvent assumes negligible losses. Then, to create specific shapes, the aluminum sheets are deep drawn which we assume to have 37% of losses Sphera Managed LCA Content and König et al. (1995).
Stainless steel sheet	Stainless steel sheets are produced from chromium steel 18/8 and a sheet rolling process for which ecoinvent assumes negligible losses. Then, to create specific shapes, the sheets are deep drawn which we assume to have the same process losses that aluminum sheet deep drawing, i.e., 37%.
Cast iron part	The cast iron is a direct product of the electric arc furnace. The final cast iron part is obtained through a process of milling the cast iron, which we assume to have 5% of losses.
Copper-plated part	Copper-plated parts are used in the RU to make up the filters. As no ecoinvent unit process covers the specific copper plating process, we model the copper-plated parts by considering only the production of copper.
Polymer part	We assume that most of the polymer parts are made of acrylonitrile-butadiene-styrene, and we model their manufacture by injection molding without losses.
Glass fiber reinforced plastic	In ecoinvent, the glass fiber-reinforced plastic is produced by injection molding of glass fiber with polyamide resin.
Sealing compound	We assume the sealing compound is polysulfide-based. In ecoinvent, such sealing compound is produced by heating a mixture of filling material, chemicals, polyurethane, and a hardening paste.

4.3 Composition of electronic sub-components

This sub-section explains how we estimate the composition of electronic sub-components of the model.

4.3.1 Printed circuit board assemblies

A PCBA typically consists of a printed circuit board (PCB) on which active and passive electronic components are mounted. As an example, Figure 28(a) and Figure 28(b) show, respectively, the front and rear view of one physical-layer board from our teardown of a BBU and highlight its main components. To model its production, we consider the manufacturing of the PCB, the manufacturing of the components, and the mounting processes. As we use ecoinvent, we model the manufacturing of the PCB with respect to its area while we model passive components with respect to their mass. Thanks to the custom unit processes developed in Section 4.1, we model the ICs with respect to their die area. We measure the die area of decapsulated ICs as in Wattiez et al. (2024) for ICs with a package area greater than 25 mm², while for smaller ICs we estimate their die area using a default die-to-package ratio of 0.5. Figure 28(c) shows pictures of ICs after decapsulation and highlights their die. We finally model the mounting processes with respect to the PCB area and we estimate the solder paste quantity using typical requirements of solder paste mass per component pin, based on EIME database. Table 11 lists and quantifies the unit processes (custom and from ecoinvent) that would be used to model the production of this specific PCBA. The background models we propose for each PCBA type in the parametric model use the same approach, considering the average composition of all disassembled PCBAs of that type.

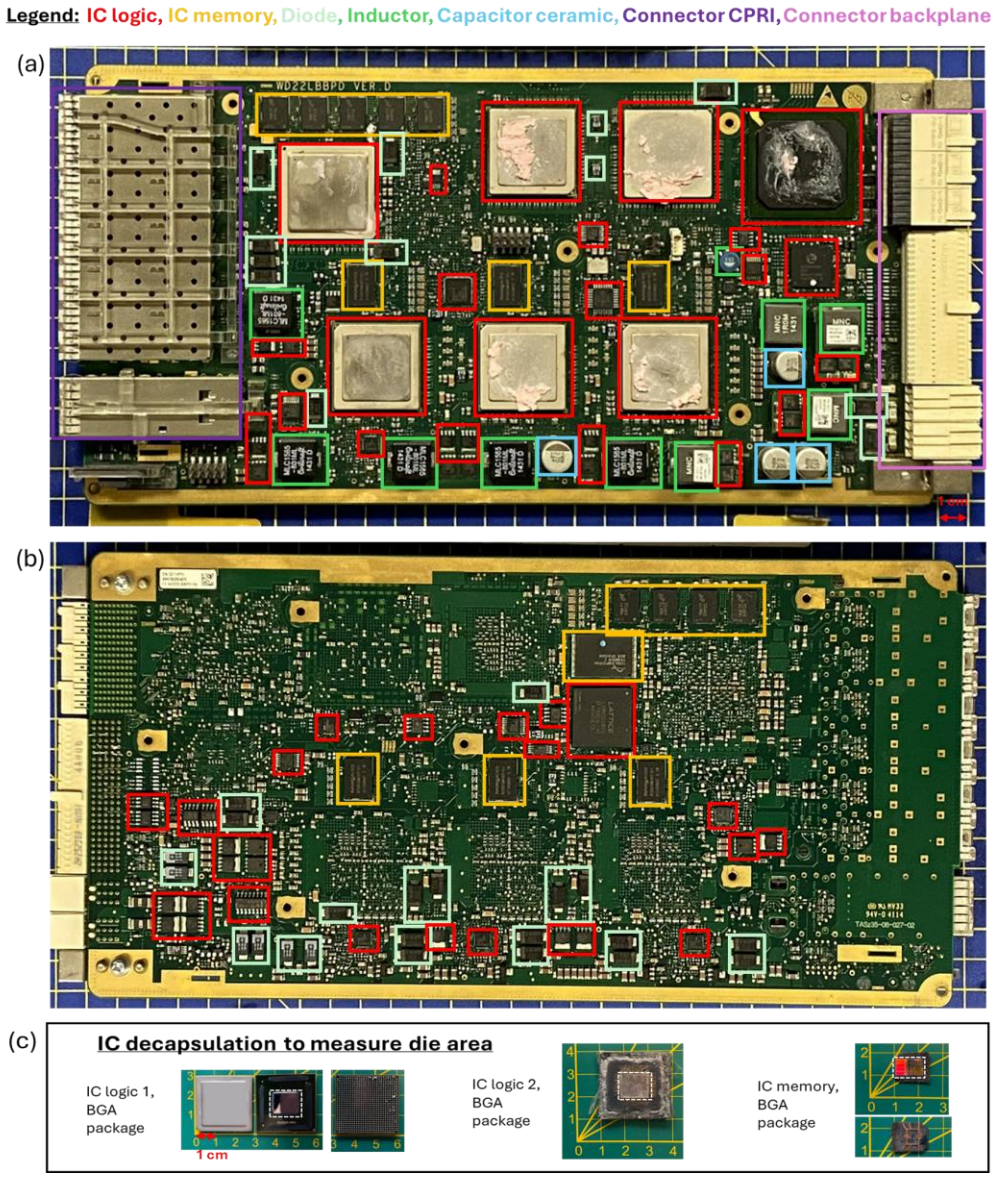

Fig. 28 Pictures of the PCBA of one physical-layer board from our teardown of a BBU with its main electronic components highlighted on its (a) front view and (b) rear view, and (c) of decapsulated IC logic and IC memory, illustrating the decapsulation of packaged ICs to measure their die area

Table 11 Unit processes with their quantity and label that would be used to model the PCBA in Figure 28

Unit process	Quantity	Label
GLO: market for printed wiring board, for surface mounting, Pb free surface	406 cm²	PCB
GLO: market for integrated circuit, logic type (*custom UCLouvain*)	21.05 cm²	ICs (logic)
GLO: market for integrated circuit, memory type (*custom UCLouvain*)	6.45 cm²	ICs (memory)
GLO: market for capacitor, electrolyte type, > 2cm height	3.2 g	Capacitors
GLO: market for capacitor, for surface-mounting	13.8 g	Capacitors
GLO: market for diode, auxilliaries and energy use	4.8 g	Other elec.
GLO: market for inductor, auxilliaries and energy use	1.0 g	Other elec.
GLO: market for inductor, ring core choke type	45.2 g	Other elec.
GLO: market for resistor, surface-mounted	2.8 g	Other elec.
GLO: market for connector backplane (*custom UCLouvain*)	34.6 g	Other elec.
GLO: market for connector CPRI (*custom UCLouvain*)	40.0 g	Other elec.
GLO: market for mounting, surface mount technology, Pb-free solder	406 cm²	Mounting
GLO: market for mounting, through-hole technology, Pb-free solder	406 cm²	Mounting
GLO: market for solder, paste, Sn95.5Ag3.9Cu0.6, for electronics industry	1.3 g	Mounting

4.3.2 Antenna elements

Figure 29 shows the mass of two different AEs measured during our own teardown of the AU. The IAF for the foreground process modeling the AE production is calculated by averaging the compositions of both AEs.

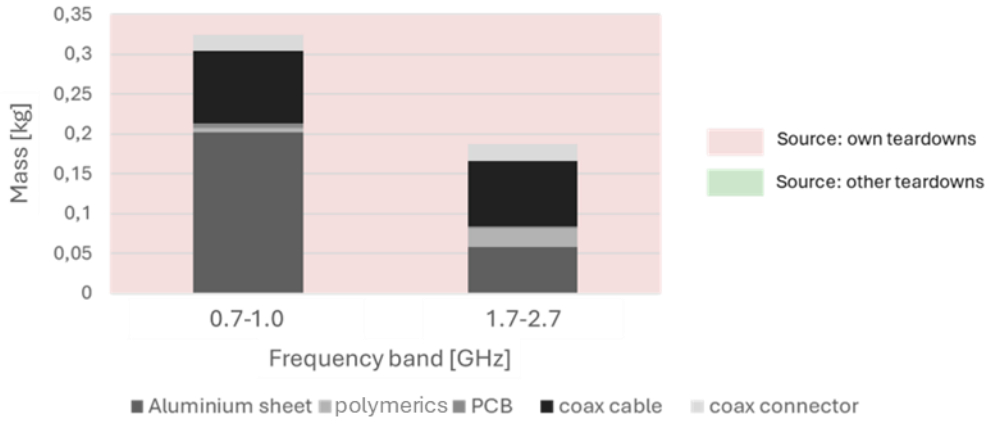

Fig. 29 Mass and composition of two antenna elements in a traditional AU emitting in two different frequency bands, including cables, connectors, a delay line system and the radiating elements

4.3.3 Cables

Figure 30 shows pictures of the teardown of a power cable from the 48 V DC power supply of the RRU, an internal coaxial cable of the AU, and an external coaxial cable. In addition to these teardowns, we use the FMDs of the *Koax24 RG-316/U* and *Molex part 897622360* for modeling respectively the power cable and the internal coaxial cables in order to identify the nature of the homogeneous materials of the cable (i.e., the metallic braid, the plastic pipes, etc.). In this work, we model the external coaxial cables by scaling the internal coaxial cable with respect to the linear density (44g/m and 94g/m for the internal and external coaxial cables respectively). As explained in the paper, we model the optical fiber exclusively based on a FMD (*Molex part 1060292001*). Note that FMDs typically model the complete cable assembly and include both end connectors, which we do not consider in this cable model, but separately in the custom connector models. In addition to the raw material, we model the processes of forming the plastic pipes and the copper braid with dedicated ecoinvent unit processes and we assume that there are no losses.

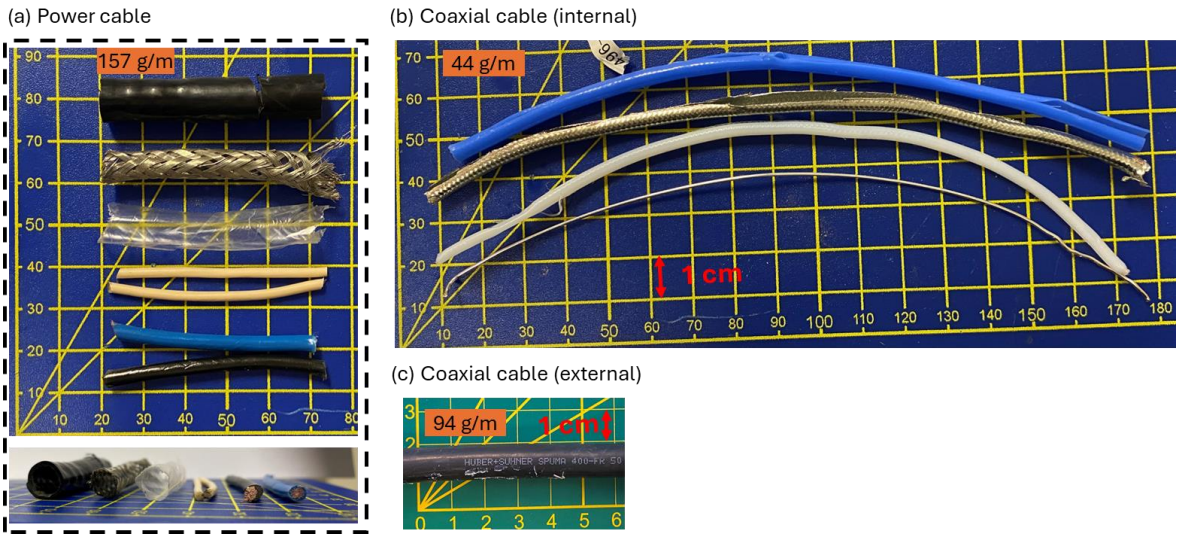

Fig. 30 Pictures of the teardown of (a) a power cable used to supply power to RRU, (b) an internal coaxial cable used to carry amplified signals in the traditional AU and (c) an external coaxial cable used to carry the amplified signals between the RU and the AU

4.4 Composition of mechanical sub-components

This sub-section explains how we estimate the composition of mechanical sub-components of the model.

4.4.1 Baseband unit

Figure 31 shows the composition of mechanical parts of several BBU boards and sub-racks. These sub-components are mainly made of steel and aluminum, whose proportions vary. Then, Figure 32 shows the composition of the complete mechanical structure in two BBU configurations, i.e., a sub-rack filled with link-layer and physical-layer boards and embedding miscellaneous functions. The two BBUs do not have the same configuration nor features. The composition of the BBU structure that we consider in our model is then the average of these two complete BBUs. The resulting average composition is: 43% stainless steel, 49% aluminum sheet, and 8% polymers.

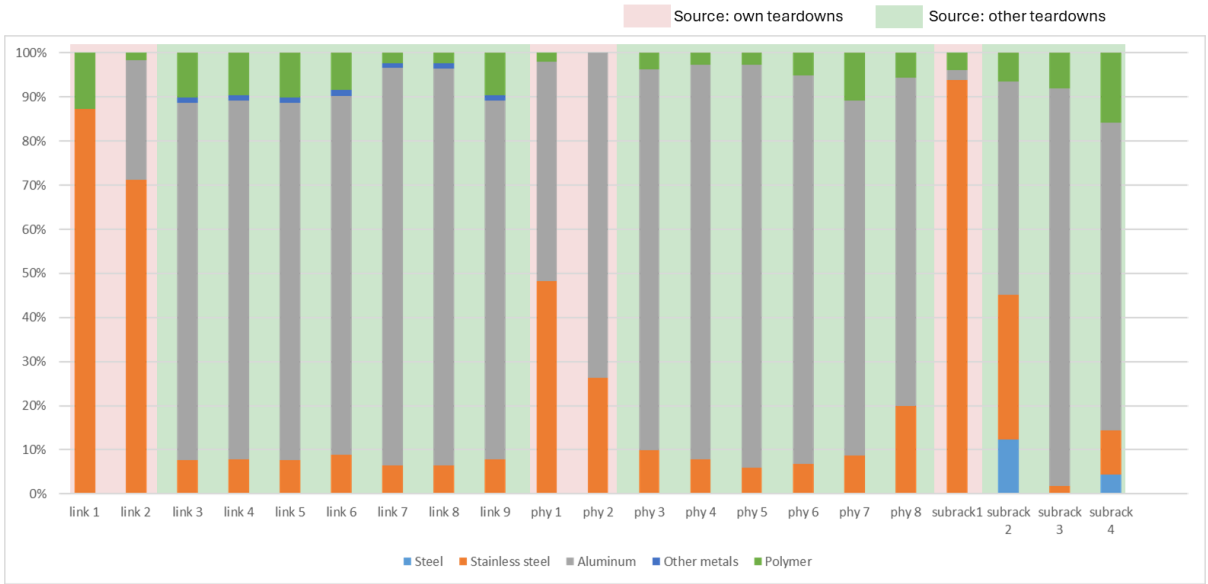

Fig. 31 Relative mass composition of mechanical parts of BBU boards and sub-racks

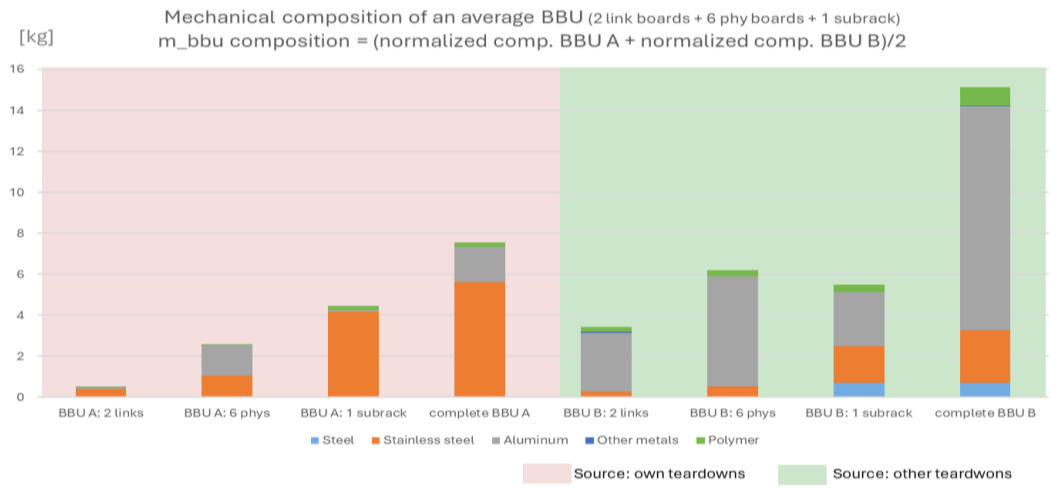

Fig. 32 Total mass of mechanical parts and complete mechanical structure in two BBU configurations

4.4.2 Radio unit

Figure 33 shows the composition of mechanical structures of several RUs. The average composition is: 83% die-cast aluminum, 8% steel, 4% stainless steel, 4% copper and 1% polymers.

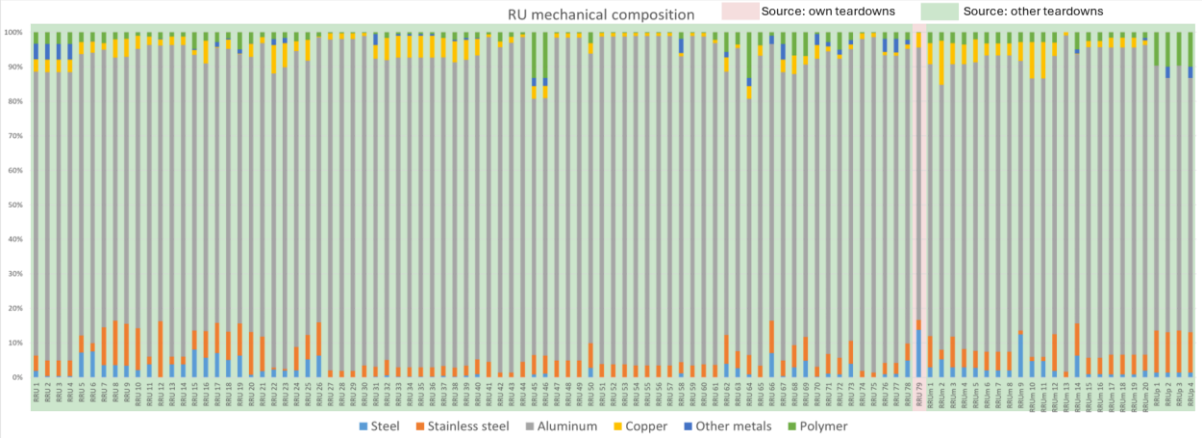

Fig. 33 Relative mass composition of mechanical structures of RUs

4.4.3 Antenna unit

Figure 34 shows the mass composition of the mechanical structure of a traditional AU based on our teardown. For an AAU, we assume that the mechanical sub-component of the AU module consists only of the polymer parts of a traditional AU because its metallic materials are allocated to the RU module.

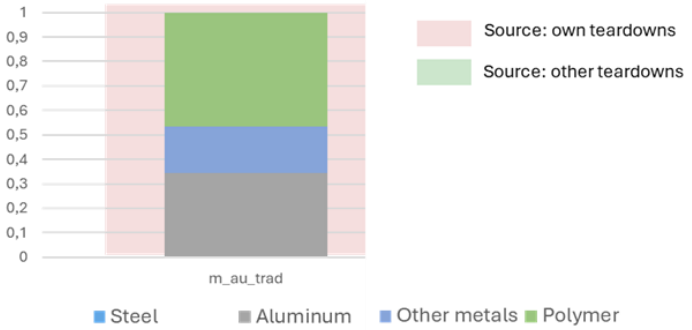

Fig. 34 Relative mass composition of the mechanical structure of one traditional AU

4.4.4 Power supply unit

We model the mechanical structure of the PSU assuming that 50% of its mass is the cabinet made of stainless steel, and the other 50% is for sub-racks with the same composition as the mechanical structure of the BBU. The resulting average composition is: 72% of stainless steel, 24% of aluminum, and 4% of polymer.

5 Uncertainty quantification

This section explains how the uncertainty factors are calculated for the FPI and the IAFs.

5.1 Uncertainty factors for the FPI

The total uncertainty factors of the FPI are expressed by their geometric standard deviation (GSD) and come from two main aspects: the variability in our data sources and the potential error made by our model. The uncertainty factors associated with these two aspects are given in Table 12 for each (type of) foreground process.

We quantify the variability factors based on the regression analyses performed on our specific data sources. Comparisons between actual values from data sources and predictions of the proposed model are shown in Figure 35 for electronic sub-components and Figure 36 for mechanical sub-components. Residuals of the predictions are represented for each observation, i.e., the difference between the exact prediction line (for which a prediction equals the actual value) and the prediction made by the proposed model. We also indicate fitting quality metrics such as RMSE and R^2, as well as the variability using the interquartile range (IQR) and the "95%" range corresponding to the interval between the 2.5th and 97.5th percentiles (hence covering 95% of observations). Lastly, we represent the fitting of relative predictions (in that case, an exact prediction equals 1) with Log-normal and Gaussian distributions.

Empirically, we find that the fitting according to a Log-normal distribution is better than with a Gaussian distribution because (i) it does not allow for negative values and (ii) its median, which is set at 1 and represents the deterministic point estimate, is generally closer to the actual median of the observations compared to the mean in the case of a Gaussian distribution. We therefore prefer to use the Log-normal distribution. In Table 12, GSDs for the production of electronic and mechanical sub-components are roughly approximated based on Figure 35 and Figure 36, with an average GSD of 1.41. The GSD of energy consumption during the use stage is estimated based on the uncertainty range given by Golard et al. (2024).

Next, we quantify the potential error by estimating minimum and maximum possible values based on our own judgments, and assuming that the interval between these two values contains 95% of the observations. Based on Limpert et al. (2001), we then determine the associated GSD knowing that GSD^2 is approximately equal to the multiplicative error factor which determines the "95%" range. In practice, when we are quite confident in our modeling of foreground process quantities, we consider that the error is approximately $\times/\div 1.25$, when we are moderately confident we consider $\times/\div 2$ factors, and when we are very poorly confident we consider $\times/\div 10$ factors. The corresponding GSD^2 are 1.25, 2 and 10, respectively. We represent these confidence degrees using a color scale in Table 12. As an example, the use of $\times/\div 10$ factors to represent the very poor confidence we have in upstream transport distance means that while we assume that the best estimate of transport distance is 1000 km, we judge that the minimum distance is 100 km, and that the maximum distance is 10 000 km.

Finally, the total GSD is calculated as

$$GSD = \exp\left(\sqrt{[\log(GSD_v)]^2 + [\log(GSD_e)]^2}\right) \quad [/]\,.$$

Table 12 Uncertainty factor derivation for FPI

(Type of) foreground process	Variability GSD_v	Error*			Total GSD
		[min ; max]	GSD_e^2	GSD_e	
electronic sub-component production	1.41	[0.8 ; 1.25]	1.25	1.12	**1.44**
mechanical sub-component production	1.41	[0.8 ; 1.25]	1.25	1.12	**1.44**
upstream/downstream transport	-	[0.1 ; 10]	10	3.16	**3.16**
distribution and collection transport	n.a.	n.a.	n.a.	n.a.	n.a.
(dis)assembly and (de-)installation	-	[0.1 ; 10]	10	3.16	**3.16**
energy consumption (in use stage)	1.25	[0.8 ; 1.25]	1.25	1.12	**1.28**
waste management routes	-	[0.5 ; 2]	2	1.41	**1.41**

*based on our own judgments

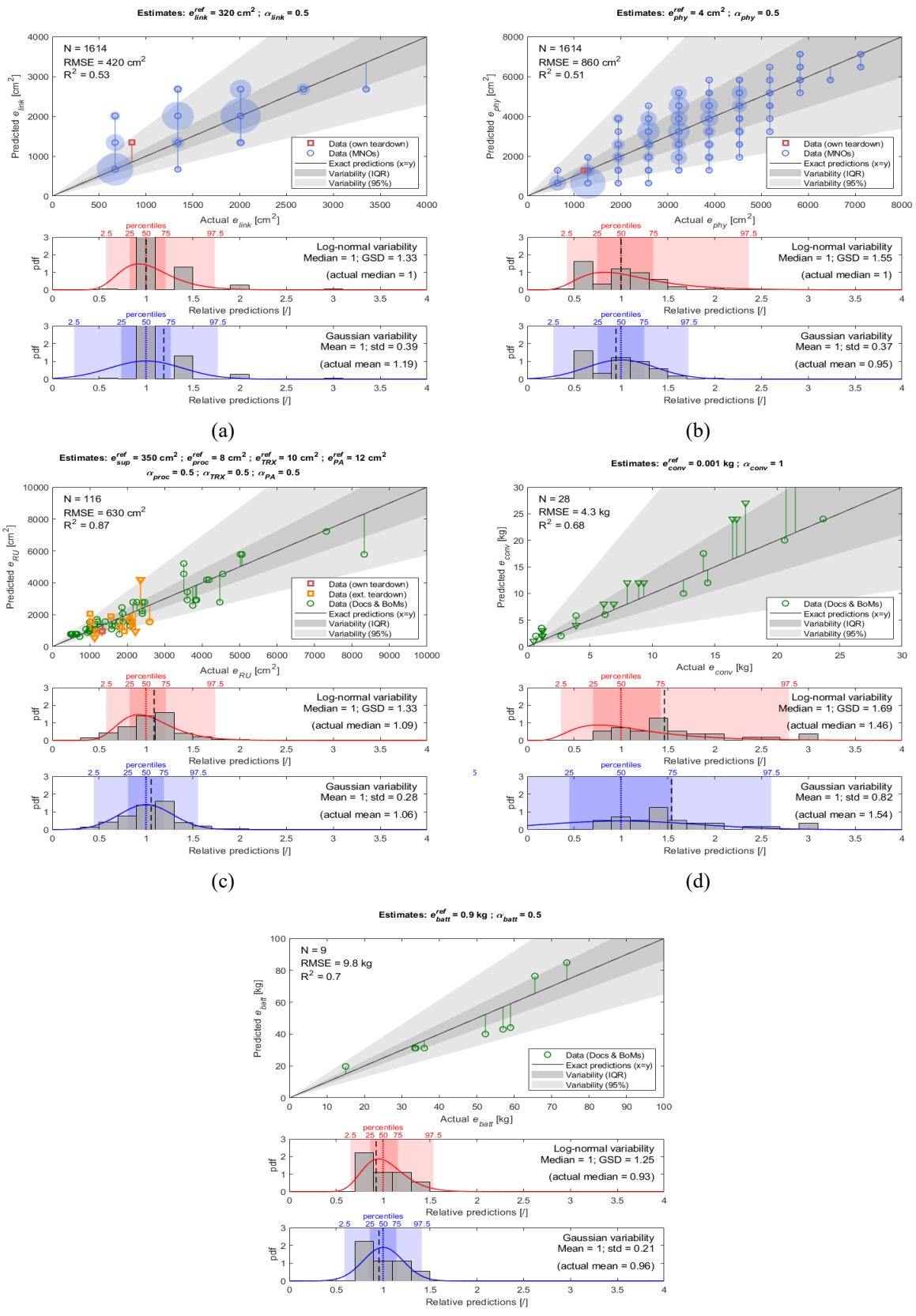

Fig. 35 Actual values from data sources vs. predictions of the proposed model (top) with distribution of relative predictions fitted with Log-normal (middle) or Gaussian (bottom) probability density functions for the quantity of electronic sub-components: (a) PCBA area of link-layer boards, (b) PCBA area of physical-layer boards, (c) PCBA area of RUs, (d) mass of power converters, and (e) mass of backup batteries

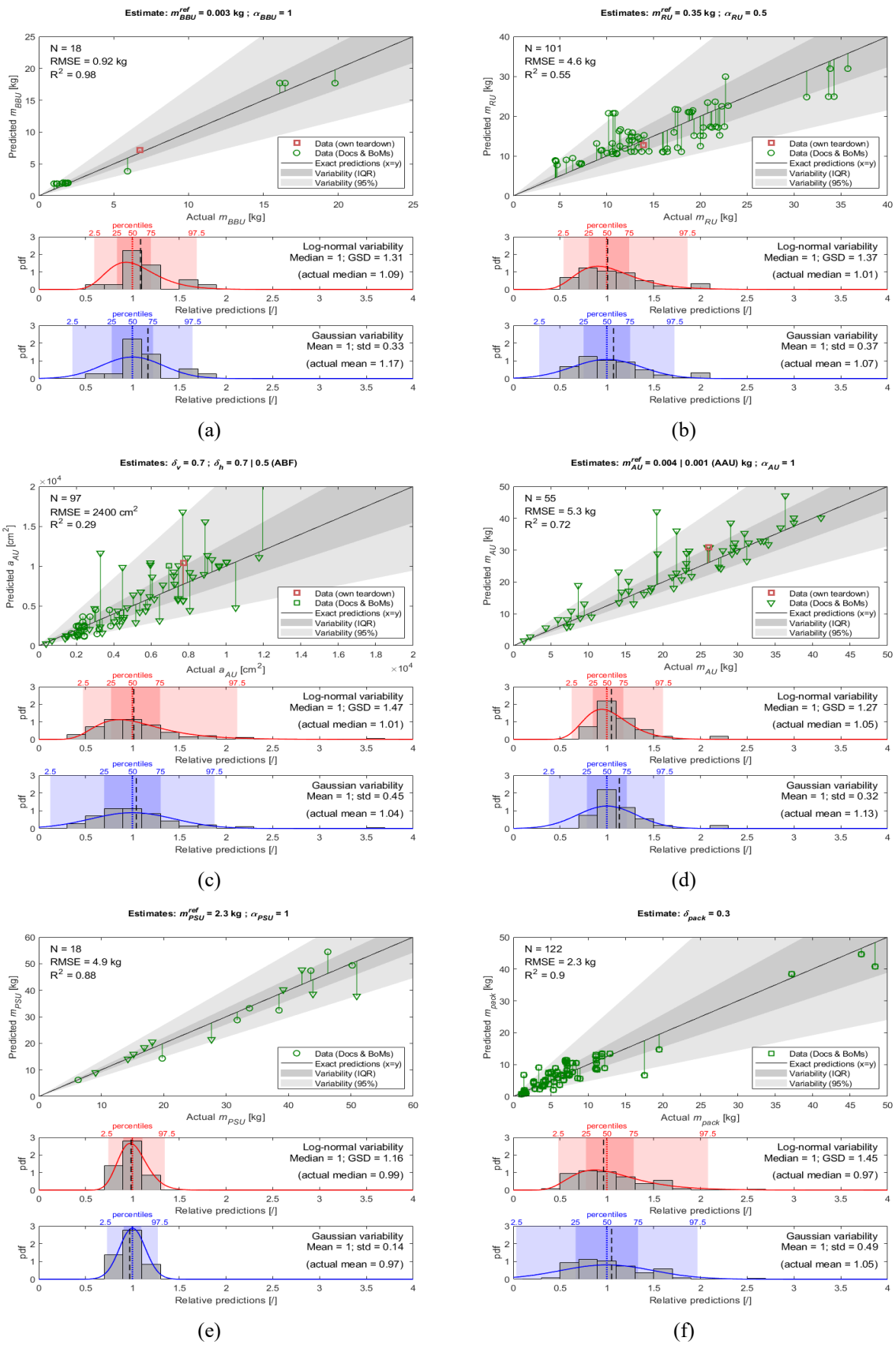

Fig. 36 Actual values from data sources vs. predictions of the proposed model (top) with distribution of relative predictions fitted with Log-normal (middle) or Gaussian (bottom) probability density functions for the quantity of mechanical sub-components: (a) mass of BBU structures, (b) mass of RU structures, (c) AU area, (d) mass of AU structure, (e) mass of PSU structure, and (f) mass of packaging

5.2 Uncertainty factors for IAFs

The total uncertainty factors of IAFs are also expressed by their GSD that could come from the variability in our data sources and the potential error made by our model. However, we cannot calculate variability factors for IAFs because they are mainly determined based on a single teardown. Instead, the error factors of IAFs capture (i) the expected variability of process composition, and (ii) the confidence we have in our modeling choices for building the background processes based on ecoinvent. The uncertainty factors associated with these two types of errors are given in Table 13 for each (type of) foreground process.

As for the FPI uncertainty, we quantify the two types of IAF errors by first estimating minimum and maximum possible values based on our own judgments, and then computing the associated GSD^2 and GSD. Yet, in this case, we estimate the potential error #1 (due to the expected variability of process composition) based on our judgement of a "best" and a "worst" case of process composition, e.g., for the BBU casing and structure, the "best" case is to use 100% of steel and the "worst" case is to use 100% of aluminum (as aluminum production has generally more impacts than steel production). Then, for the potential error #2, when we are quite confident in our modeling choices for building the background processes, we consider that the error is approximately $\times/\div 1.25$, when we are moderately confident we consider $\times/\div 2$ factors, when we are poorly confident we consider $\times/\div 3.16$ factors (i.e., an order of magnitude range), and when we are very poorly confident we consider $\times/\div 10$ factors. The corresponding GSD^2 are then 1.25, 2, 3.16 and 10, respectively. We also represent these confidence degrees using a color scale in Table 13.

The total GSD is also calculated as

$$GSD = \exp\left(\sqrt{[\log(GSD_1)]^2 + [\log(GSD_2)]^2}\right) \quad [/]\,.$$

Table 13 Uncertainty factor derivation for IAFs

(Type of) foreground process	Error* #1 (expected variability in the composition of foreground process)			Error* #2 (confidence in our modeling of background processes based on ecoinvent)			Total GSD
	[min ; max]	GSD_1^2	GSD_1	[min ; max]	GSD_2^2	GSD_2	
electronic sub-component production	[0.5 ; 2]	2	1.41	[0.8 ; 1.25]	1.25	1.12	**1.44**
mechanical sub-component production	[0.32 ; 3.16]	3.16	1.78	[0.8 ; 1.25]	1.25	1.12	**1.80**
upstream/downstream transport	[0.32 ; 3.16]	3.16	1.78	[0.8 ; 1.25]	1.25	1.12	**1.80**
distribution and collection transport	[0.8 ; 1.25]	1.25	1.12	[0.8 ; 1.25]	1.25	1.12	**1.17**
(dis)assembly and (de-)installation	[0.8 ; 1.25]	1.25	1.12	[0.8 ; 1.25]	1.25	1.12	**1.17**
energy consumption (in use stage)	[0.8 ; 1.25]	1.25	1.12	[0.8 ; 1.25]	1.25	1.12	**1.17**
waste management routes	[0.32 ; 3.16]	3.16	1.78	[0.1 ; 10]	10	3.16	**3.62**

*based on our own judgments

6 Base station capacity and coverage

This section explains how to calculate the data throughput capacity and coverage of the typical BS configurations proposed in Table 4 of the core paper. These metrics are used to represent the useful wireless communication service provided by the BSs.

6.1 Capacity computation

In this work, we define the data throughput capacity as the maximum total data rate achievable in DL over one sector for a given BS configuration. This is a proxy for the wireless communication service provided by the BS in the context of broadband Internet access. Although this is a common representation of the BS service, other metrics could also be used to represent the BS service(s), targeting, e.g., latency, the total number of users (human or machine) that can be connected, service reliability, etc. The total capacity of a BS can serve a single user or several users, depending on the number of active users in its sector and on its scheduling policy (controlled by the BBU). We calculate the BS capacity on a single sector (and not on the sum of all its sectors, typically three) because a single user could not connect to several BS sectors at the same time to benefit from the aggregation of the physical resources of several sectors (which use, moreover, the same time and frequency resources). On the other hand, we consider that it is possible for a single user to aggregate all the physical resources of a BS in a single sector, thanks to multi-RAT, carrier aggregation and spatial data layer multiplexing (thanks to MIMO).

The data throughput capacity of a BS is therefore calculated by aggregating all spatial data layers on all frequency bands for all communication protocols in a single sector, as

$$C = \sum_{i=1}^{N_B} \gamma_i N_{L,i} \left(\frac{B_i}{B^\star}\right) \quad [\text{Mbps}] \,,$$

where γ_i is the spectral efficiency of frequency band i. We assume a maximum spectral efficiency of 4 bps/Hz in DL for all frequency bands and communication protocols. This is not the strict peak DL spectral efficiency achievable in 4G-LTE and 5G-NR, respectively 6 bps/Hz (in 64QAM) and 8 bps/Hz (in 256QAM), but we consider it to be a realistic maximum DL spectral efficiency in practice, well beyond the typical average spectral efficiency over the whole cell coverage (around 2 bps/Hz). For example, the total throughput capacity of the 3-bands configuration is calculated by multiplying its total bandwidth of $2 \times 10 + 2 \times 20 + 4 \times 20 = 140$ MHz by the spectral efficiency of 4 bps/Hz, giving 560 Mbps. The spectral efficiency of 4 bps/Hz is also used in Section 6.2 to calculate the BS coverage and can be seen as a parameter defining the BS communication service.

A better proxy for the BS service could be the average capacity per user, considering the user distribution over the sector and the specific radio channel path loss for each user and each frequency band (see the path loss model in Section 6.2), and considering specific maximum spectral efficiencies per communication protocol. We could also include UL in addition to DL in the overall capacity calculation, even if, so far, the quality of service for mobile Internet access has been defined mainly on the basis of DL traffic, which currently represents up to 90% of total mobile data traffic. However, we prefer to keep the capacity calculations simple in this work and leave detailed analysis to readers who seek greater precision.

6.2 Coverage computation

To determine the coverage of a BS configuration, we start by computing the required sensitivity of the user equipment (UEs) to receive the BS signals. We then impose that the power received by the UE is at least equal to its sensitivity, and from this we derive the maximum transmission distance in the worst case, i.e., when the sensitivity is exactly equal to the received power (and therefore when the UE is farthest from the BS). This distance depends on the radio channel propagation, which in turn depends on the BS configuration.

The sensitivity of a UE is the minimum receive power level required to provide a given data throughput. The sensitivity power level, denoted $P_{sens,dB}$ and expressed in dBm/Hz, is calculated by summing the thermal noise level in dBm/Hz with the noise figure (NF) in dB and the signal-to-noise ratio (SNR) in dB as

$$P_{sens,dB} = \text{Noise}_{dB} + \text{NF}_{dB} + \text{SNR}_{dB} \quad [\text{dBm/Hz}] \,.$$

The SNR required to transmit data with a given spectral efficiency γ is calculated using the theoretical channel capacity given by the Shannon-Hartley theorem as

$$\gamma = \log_2(1 + \text{SNR}) \quad [\text{bps/Hz}] \,.$$

The resulting SNR is then

$$\text{SNR}_{dB} = 10 \log_{10}(2^\gamma - 1) \quad [\text{dB}] \,,$$

which is about 12 dB with a spectral efficiency of 4 bps/Hz (as defined in the previous section). Knowing that the thermal noise power level at 300 K (around 27°C) is equal to -174 dBm/Hz and that the typical noise figure of a UE is 7 dB, we can then compute $P_{sens,dB} = -174 + 12 + 7 = -155$ dBm/Hz.

The power level per layer received by the UE, denoted $P_{RX,dB}^{layer}$ and expressed in dBm/Hz, is calculated using the link budget: first, the maximum TX power level per layer, denoted $P_{TX,dB}^{layer}$ and expressed in dBm/Hz, is summed with the TX and RX antenna gains, in dB, and then, the radio channel path loss (PL), also in dB, is subtracted as

$$P_{RX,dB}^{layer} = P_{TX,dB}^{layer} + G_{TX,dB} + G_{RX,dB} - \mathrm{PL}_{dB} \quad [\mathrm{dBm/Hz}] .$$

The maximum TX power level per layer is computed as

$$P_{TX,dB}^{layer} = 10 \log_{10} \left(\frac{\frac{N_{TX}}{N_L} P_{TX} \cdot 10^3}{B \cdot 10^6} \right) \quad [\mathrm{dBm/Hz}] ,$$

where the maximum TX power per layer and the bandwidth are respectively expressed in mW and Hz with the factors 10^3 and 10^6. The whole is then converted into logarithmic units. The TX antenna gain used to approximate the BS coverage is the total antenna gain $G_{TX,dB}$ for the BS configuration, and the RX antenna gain is set to be $G_{RX,dB} = 0$ dB, considering an omnidirectional RX antenna. With ABF, the maximum total antenna gain is achieved when all spatial data layers are used to transmit the same (pre-coded) data stream in order to form a narrower beam and reach the farthest UEs. Hence, assuming the antenna gain of a single sub-array to estimate the BS coverage would be too pessimistic. However, this conflicts with the capacity calculation described hereabove, which assumes that all spatial data layers transmit different data streams in order to achieve full multiplexing capability. Consequently, full coverage and full capacity cannot be achieved simultaneously with ABF, requiring a more careful analysis to take this into account.

The path loss computation follows the modified "COST231-Hata" radio channel propagation model given by Khan (2009) in an urban scenario. This is expressed by

$$\mathrm{PL}_{dB} = (44.9 - 6.55 \log_{10}(h_{BS})) \cdot \log_{10}(d) + L(f, h_{BS}, h_{UE}) \quad [\mathrm{dB}] \text{ and}$$

$$L(f, h_{BS}, h_{UE}) = 45.5 + (35.46 - 1.1 h_{UE}) \cdot \log_{10}(f \cdot 10^3) - 13.82 \log_{10}(h_{BS}) + 0.7 h_{UE} \quad [\mathrm{dB}] ,$$

where h_{BS} and h_{UE} are respectively the heights of the BS and the UE in m, d is the distance from the BS in km, and f is the carrier frequency expressed in MHz with the factor 10^3. We assume $h_{BS} = d_{AU}$ and $h_{UE} = 1.5$ m. For instance, this propagation model says that the path loss at 1 km for a BS with $h_{BS} = 25$ m is 125, 137 or 147 dB for respectively a carrier frequency of 0.8, 1.8 or 3.5 GHz. This means that for the same coverage, we need to transmit 22 dB more at 3.5 GHz than at 0.8 GHz, which can be achieved with greater antenna gain, primarily through high beamforming gain, and with increased TX power.

To calculate the BS coverage, we set $P_{sens,dB} = P_{RX,dB}$, which gives

$$-155 = P_{TX,dB} + G_{TX,dB} - (44.9 - 6.55 \log_{10}(h_{BS})) \cdot \log_{10}(d_{cov}) - L(f, h_{BS}, h_{UE}) ,$$

where d_{cov} is the BS coverage range in km. We can then derive d_{cov} as

$$d_{cov} = 10^{\left(\frac{P_{TX,dB} + G_{TX,dB} - L(f, h_{BS}, h_{UE}) + 155}{44.9 - 6.55 \log_{10}(h_{BS})} \right)} \quad [\mathrm{km}] .$$

Considering the coverage range as the radius of BS sectors, we finally estimate the BS coverage area as

$$\mathcal{A}_{cov} = \pi d_{cov}^2 \quad [\mathrm{km^2}] .$$

If there are several frequency bands, we define the BS coverage as the smallest coverage among all its frequency bands (i.e., the one with the highest frequency carrier), as this is the most constraining band to guarantee the spectral efficiency of 4 bps/Hz. Once again, we leave detailed analysis to readers who require more precision.

7 Additional results

This final section presents additional results from the LCA study to complement some of the analyses and interpretations formulated in the core paper.

7.1 IAF results

Figure 37 shows the contribution of carbon dioxide (CO_2) to GWP for all foreground processes. We observe that CO_2 accounts for around 85% of the GWP on average, the remainder being mainly due to methane emissions from fossil fuels. The production of electronic sub-components, particularly those made up of many ICs such as BBU boards, have a low CO_2 contribution due to the fluorinated gases required for their manufacture.

Figure 38 shows the IAFs for the "resource use – minerals and metals" impact category through the abiotic resource depletion potential (ADP) indicator. Compared with GWP, the impact of using copper is much more pronounced, e.g., in PSU power converters, RU filters, power cables, but also in the transmission and distribution networks of electrical grids. In contrast, the use of fossil polymers and the combustion of fossil fuels are negligible for ADP. Another impact category covers separately the use of fossil resources (namely RUf).

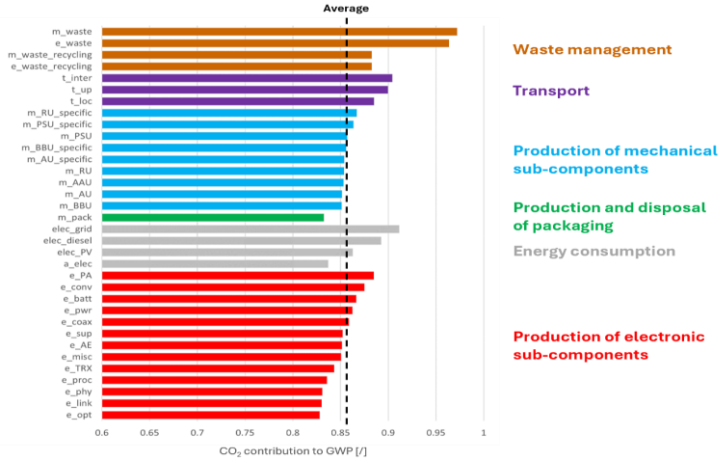

Fig. 37 Contribution of CO_2 to GWP for all foreground processes grouped by type and ranked in descending order of CO_2 contribution. The average CO_2 contribution is represented by the dashed line

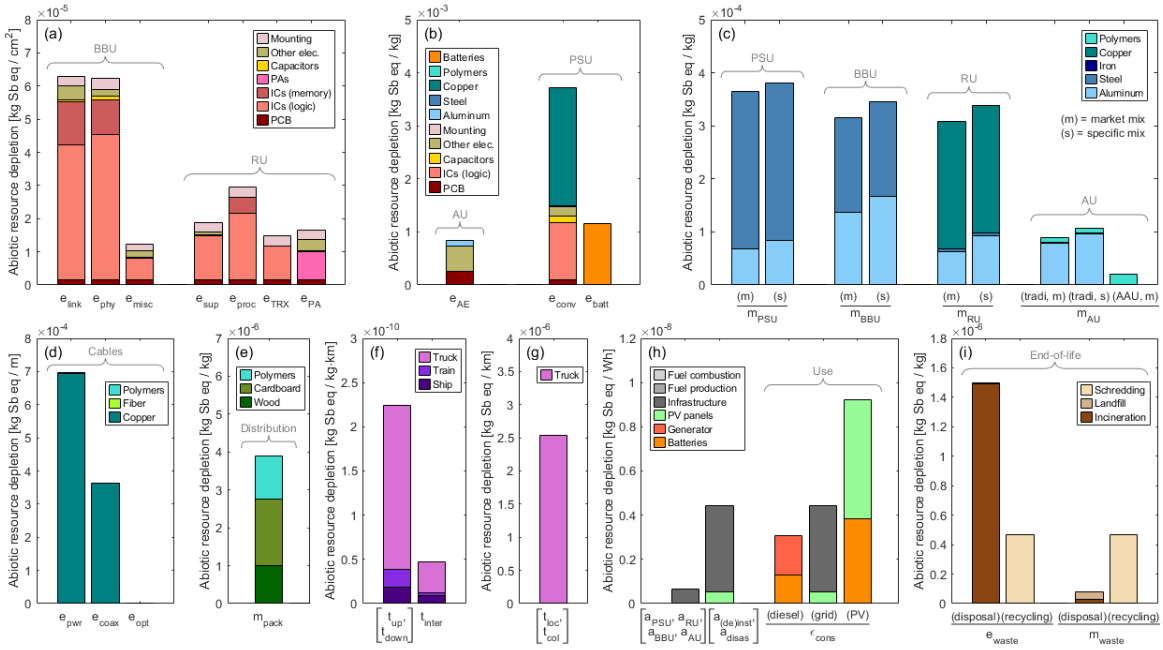

Fig. 38 Abiotic resource depletion potential of all foreground processes for (a) printed circuit board assembly production, (b) other electronic production, (c) mechanical structure production, (d) cable production, (e) packaging production and disposal, (f) freight transport, (g) local transport, (h) electricity consumption, and (i) waste management routes. Some impact factors apply to several processes (in brackets), while other processes may be linked to different impact factors depending on the model options (in parentheses)

7.2 Assessment of all life-cycle stages

Figure 39 and Figure 40 present the results for the distribution and end-of-life stages, respectively. Figure 39(a) and Figure 40(a) show the impacts for all categories in the illustrative 3-bands configuration, whereas Figure 39(b) and Figure 40(b) focus on the GWP and Figure 39(c) and Figure 40(c) on the ADP and extend the results to all typical BSs configurations (see Table 4 in the core paper). This illustrates that local distribution transport dominates GWP and ADP, as there is no longer any allocation of freight by mass of goods transported. The same applies to the transport of local collection at end-of-life. For the distribution stage, packaging production can also have a significant impact on land use due to the use of wood and cardboard from trees (LU) and on water use (WU). For the end-of-life stage, incineration, particularly of electronic sub-components, has a significant impact on human toxicity and eco-toxicity indicators (HTc, HTnc and ET).

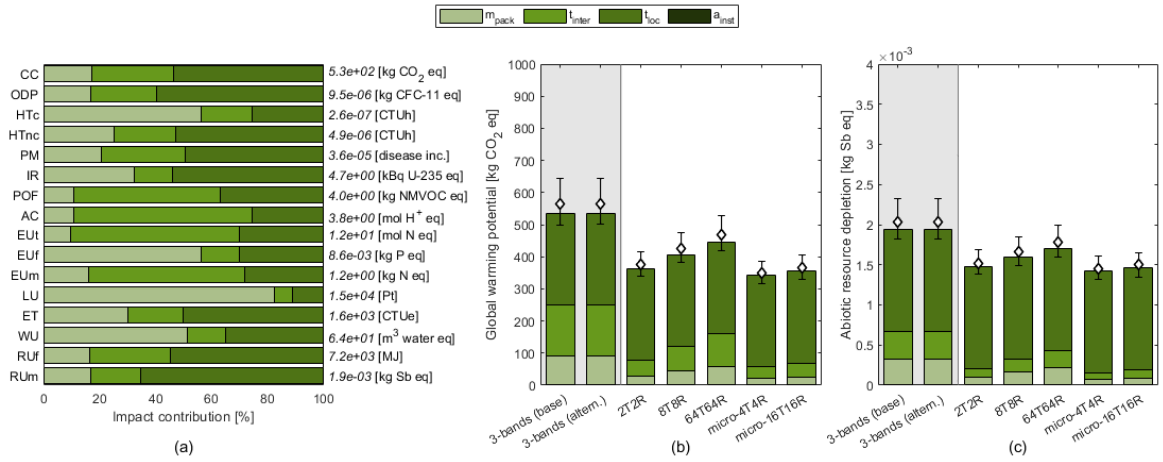

Fig. 39 Results of the distribution stage (a) in the 3-bands configuration for all Environmental Footprint categories: climate change (CC), ozone depletion (ODP), human toxicity – cancer (HTc) and – non-cancer (HTnc), particulate matter (PM), ionizing radiation (IR), photochemical ozone formation (POF), acidification (AC), eutrophication – terrestrial (EUt), – freshwater (EUf) and – marine (EUm), land use (LU), ecotoxicity freshwater (ET), water use (WU), and resource use – fossils (RUf) and – minerals and metals (RUm), and in all typical base station configurations (b) for the global warming potential, and (c) for the abiotic resource depletion potential

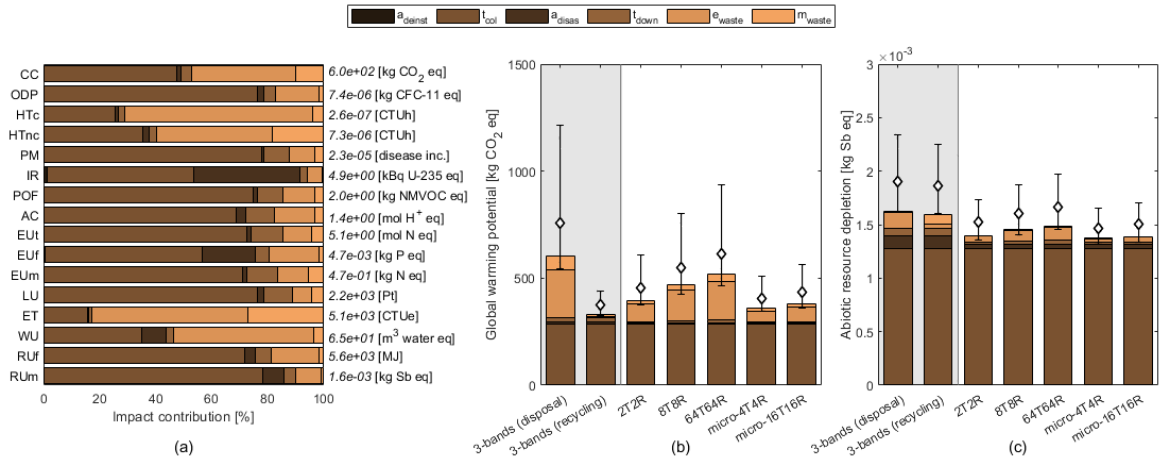

Fig. 40 Results of the end-of-life stage (a) in the 3-bands configuration for all Environmental Footprint categories: climate change (CC), ozone depletion (ODP), human toxicity – cancer (HTc) and – non-cancer (HTnc), particulate matter (PM), ionizing radiation (IR), photochemical ozone formation (POF), acidification (AC), eutrophication – terrestrial (EUt), – freshwater (EUf) and – marine (EUm), land use (LU), ecotoxicity freshwater (ET), water use (WU), and resource use – fossils (RUf) and – minerals and metals (RUm), and in all typical base station configurations (b) for the global warming potential, and (c) for the abiotic resource depletion potential

Figure 41 shows the results for all life-cycle stages of the illustrative 3-bands configuration. Figure 41(a) shows the impacts for all categories considering the market mix of raw materials, the electricity grid supply and the disposal waste management route. We can see that the use stage is clearly the hotspot of this BS configuration (from over 50% to almost 100% of total impacts), while the distribution and end-of-life stages never contribute more than 5% to total impacts, whatever the category. The production stage can also contribute significantly, especially in terms of resource use - minerals and metals (RUm), human toxicity indicators (HTc, HTnc, PM) and eco-toxicity (ET). Figure 41(b) and Figure 41(c) compare all options of this BS configuration for respectively the GWP and the ADP. In terms of GWP, the use stage always dominates the total impacts, whatever the power source chosen for the energy supply of this macro-BS: 98% with the diesel generator, 90% with the electric grid, and 75% with an isolated PV system (which divides the carbon intensity of the electricity consumed by ×10 compared to the diesel generator). In contrast, the use of an isolated PV system with battery storage increases threefold the ADP of the use stage, from a contribution of 50% to 70% of total impacts. The use of a specific mix of raw materials containing almost exclusively recycled aluminum does not reduce the ADP of the production stage.

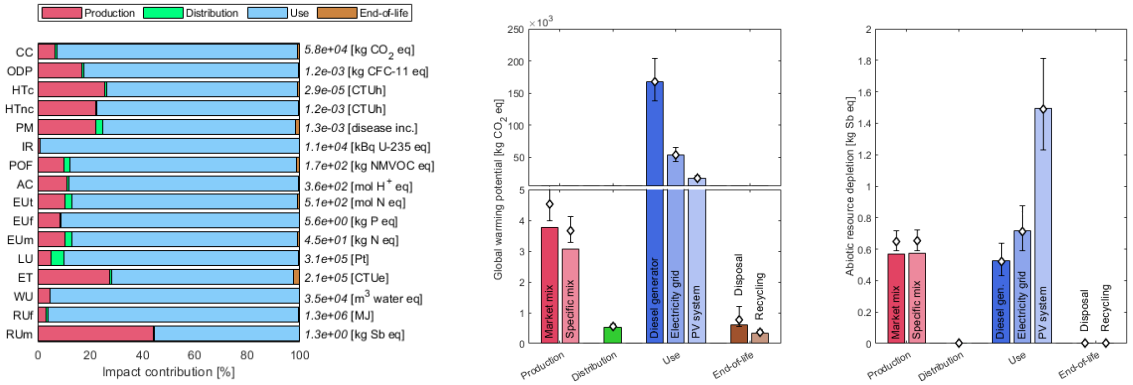

(a) (b) (c)

Fig. 41 Results for all life-cycle stages of the 3-bands configuration (a) in all Environmental Footprint categories considering the market mix of raw materials, the electricity grid supply and the disposal waste management route, and comparing all options (b) for the global warming potential, and (c) for the abiotic resource depletion potential

References

AISG (2018) Antenna port colour coding V3.2.1. AISG Standard. https://aisg.org.uk/file/AISG-Antenna-Port-Color-Coding-v3.2.1.pdf. Accessed 15 October 2024

Boakes L, Bardon MG, Schellekens V, Liu IY, Vanhouche B, Mirabelli G et al. (2023) Cradle-to-gate life cycle assessment of CMOS logic technologies. IEEE International Electron Devices Meeting (IEDM). https://doi.org/10.1109/IEDM45741.2023.10413725

Boyd SB (2011) Life-cycle assessment of semiconductors. Springer, New York. https://doi.org/10.1007/978-1-4419-9988-7

Delos P, Broughton B, Kraft J (2020) Phased array antenna patterns – Part 1: Linear array beam characteristics and array factor. Analog Devices. https://www.analog.com/media/en/analog-dialogue/volume-54/number-2/phased-array-antenna-patterns-part-1-linear-array-beam-characteristics-and-array-factor.pdf. Accessed 15 October 2024

Golard L, Agram Y, Rottenberg F, Quitin F, Bol D, Louveaux J (2024) A parametric power model of multi-band sub-6 GHz cellular base stations using on-site measurements. IEEE 35th Annual International Symposium on Personal, Indoor and Mobile Radio Communications (PIMRC). http://hdl.handle.net/2078.1/289070

Hischier R, Classen M, Lehmann M, Scharnhorst W (2007) Life cycle inventories of electric and electronic equipment: Production, use and disposal. Ecoinvent documentation

Khan F (2009) LTE for 4G mobile broadband – Air interface technologies and performance. Cambridge University Press, United Kingdom. https://doi.org/10.1017/CBO9780511810336

König W, Klocke F (1995) Fertigungsverfahren: Blechbearbeitung. Springer, Germany. https://doi.org/10.1007/978-3-662-11733-0

Limpert E, Stahel W A, Abbt M (2001) Log-normal distributions across the sciences: Keys and clues: on the charms of statistics, and how mechanical models resembling gambling machines offer a link to a handy way to characterize log-normal distributions, which can provide deeper insight into variability and probability - Normal or log-normal: That is the question. Bioscience 51(5):341-352. https://doi.org/10.1641/0006-3568(2001)051[0341:LNDATS]2.0.CO;2

Pirson T, Delhaye TP, Pip AG, Le Brun G, Raskin JP, Bol D (2022) The environmental footprint of IC production: review, analysis, and lessons from historical trends. IEEE Trans Semicond Manuf 36(1):56-67. https://doi.org/10.1109/TSM.2022.3228311

Prakash S, Liu R, Schischke K, Stobbe L, Gensch CO (2013) Schaffung einer datenbasis zur ermittlung ökologischer wirkungen der produkte der informations-und kommunikationstechnik (IKT). Unweltbundesamt. https://www.umweltbundesamt.de/sites/default/files/medien/378/publikationen/texte_82_2013_janssen_informationstechnik_teil_c.pdf. Accessed 15 October 2024

Tahseen HU, Mescia L, Catarinucci L (2023) A survey of five generations of MIMO multiband base station antennas. Radio Sci 58(7):e2023RS007725. https://doi.org/10.1029/2023RS007725

Wattiez A, Dethienne R, Collin AS, Bol D (2024) Parametric modeling for improved die area estimation in the life cycle assessment of electronic systems. Electronics Goes Green (EGG). http://hdl.handle.net/2078.1/290518

Wernet G, Bauer C, Steubing B, Reinhard J, Moreno-Ruiz E, Weidema B (2016) The ecoinvent database version 3 (part I): Overview and methodology. Int J Life Cycle Ass 21:1218-1230. https://doi.org/10.1007/s11367-016-1087-8

Williams ED, Ayres RU, Heller M (2002) The 1.7 kilogram microchip: Energy and material use in the production of semiconductor devices. Environ Sci Technol 36(24):5504-5510. https://doi.org/10.1021/es025643o